Astronomy & Astrophysics

The Tarantula Massive Binary Monitoring

II. First SB2 orbital and spectroscopic analysis for the Wolf-Rayet binary R145[*]

T. Shenar[1], N. D. Richardson[2], D. P. Sablowski[3], R. Hainich[1], H. Sana[4], A. F. J. Moffat[5], H. Todt[1], W.-R. Hamann[1],
L. M. Oskinova[1], A. Sander[1], F. Tramper[6], N. Langer[7], A. Z. Bonanos[8], S. E. de Mink[9], G. Gräfener[10],
P. A. Crowther[11], J. S. Vink[10], L. A. Almeida[12, 13], A. de Koter[4, 9], R. Barbá[14], A. Herrero[15], and K. Ulaczyk[16]

[1] Institut für Physik und Astronomie, Universität Potsdam, Karl-Liebknecht-Str. 24/25, 14476 Potsdam, Germany
e-mail: shtomer@astro.physik.uni-potsdam.de
[2] Ritter Observatory, Department of Physics and Astronomy, The University of Toledo, Toledo, OH 43606-3390, USA
[3] Leibniz-Institut für Astrophysik Potsdam, An der Sternwarte 16, 14482 Potsdam, Germany
[4] Institute of Astrophysics, KU Leuven, Celestijnenlaan 200 D, 3001 Leuven, Belgium
[5] Département de physique and Centre de Recherche en Astrophysique du Québec (CRAQ), Université de Montréal, CP 6128,
Succ. Centre-Ville, Montréal, Québec, H3C 3J7, Canada
[6] European Space Astronomy Centre (ESA/ESAC), PO Box 78, 28691 Villanueva de la Cañada, Madrid, Spain
[7] Argelander-Institut für Astronomie der Universität Bonn, Auf dem Hügel 71, 53121 Bonn, Germany
[8] IAASARS, National Observatory of Athens, 15236 Penteli, Greece
[9] Anton Pannenkoek Astronomical Institute, University of Amsterdam, 1090 GE Amsterdam, The Netherlands
[10] Armagh Observatory, College Hill, Armagh, BT61 9DG, UK
[11] Department of Physics and Astronomy, University of Sheffield, Sheffield S3 7RH, UK
[12] Instituto de Astronomia, Geofísica e Ciências, Rua do Matão 1226, Cidade Universitária São Paulo, SP, Brasil
[13] Dep. of Physics & Astronomy, Johns Hopkins University, Bloomberg Center for Physics and Astronomy, 3400N Charles St, USA
[14] Departamento de Física y Astronomía, Universidad de la Serena, Av. Juan Cisternas 1200 Norte, La Serena, Chile
[15] Instituto de Astrofísica, Universidad de La Laguna, Avda. Astrofísico Francisco Sánchez s/n, 38071 La Laguna, Tenerife, Spain
[16] Warsaw University Observatory, Al. Ujazdowskie 4, 00-478 Warszawa, Poland

ABSTRACT

We present the first SB2 orbital solution and disentanglement of the massive Wolf-Rayet binary R145 ($P = 159$ d) located in the Large Magellanic Cloud. The primary was claimed to have a stellar mass greater than $300\,M_\odot$, making it a candidate for being the most massive star known to date. While the primary is a known late-type, H-rich Wolf-Rayet star (WN6h), the secondary has so far not been unambiguously detected. Using moderate-resolution spectra, we are able to derive accurate radial velocities for both components. By performing simultaneous orbital and polarimetric analyses, we derive the complete set of orbital parameters, including the inclination. The spectra are disentangled and spectroscopically analyzed, and an analysis of the wind-wind collision zone is conducted. The disentangled spectra and our models are consistent with a WN6h type for the primary and suggest that the secondary is an O3.5 If*/WN7 type star. We derive a high eccentricity of $e = 0.78$ and minimum masses of $M_1 \sin^3 i \approx M_2 \sin^3 i = 13 \pm 2\,M_\odot$, with $q = M_2/M_1 = 1.01 \pm 0.07$. An analysis of emission excess stemming from a wind-wind collision yields an inclination similar to that obtained from polarimetry ($i = 39 \pm 6°$). Our analysis thus implies $M_1 = 53^{+40}_{-20}$ and $M_2 = 54^{+40}_{-20}\,M_\odot$, excluding $M_1 > 300\,M_\odot$. A detailed comparison with evolution tracks calculated for single and binary stars together with the high eccentricity suggests that the components of the system underwent quasi-homogeneous evolution and avoided mass-transfer. This scenario would suggest current masses of $\approx 80\,M_\odot$ and initial masses of $M_{\mathrm{i},1} \approx 105$ and $M_{\mathrm{i},2} \approx 90\,M_\odot$, consistent with the upper limits of our derived orbital masses, and would imply an age of ≈ 2.2 Myr.

Key words. binaries: spectroscopic – stars: Wolf-Rayet – stars: massive – Magellanic Clouds – stars: individual: R 145 – stars: atmospheres

1. Introduction

Ever-growing efforts are made to discover the most massive stars in the Universe (e.g., Massey & Hunter 1998; Schnurr et al. 2008a; Bonanos 2009; Bestenlehner et al. 2011; Tramper et al. 2016). Because of their extreme influence on their environment, understanding the formation, evolution, and death of massive

stars is imperative for a multitude of astrophysical fields. Establishing the upper mass limit for stars is one of the holy grails of stellar physics, laying sharp constraints on the initial mass function (Salpeter 1955; Kroupa 2001) and massive star formation (Bonnell et al. 1997; Oskinova et al. 2013). Current estimates for an upper mass limit range from $\approx 120\,M_\odot$ (e.g., Oey & Clarke 2005) to $\gtrsim 300\,M_\odot$ (e.g., Crowther et al. 2010; Schneider et al. 2014a; Vink 2015).

However, the only reliable method to weigh stars is by analyzing the orbits of stars in binaries (Andersen 1991; Torres et al. 2010). This is especially crucial for massive Wolf-Rayet (WR)
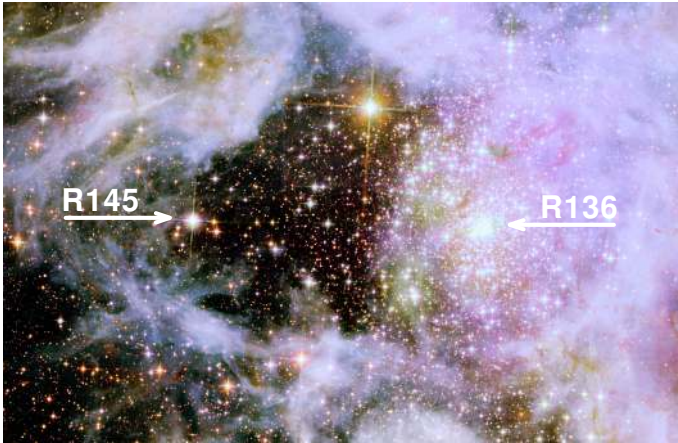

Fig. 1. Sky area around R145 (credit: NASA, ESA, E. Sabbi, STScI). The image was obtained using the *Hubble* Space Telescope's (HST) WFC3 and ACS cameras in filters that roughly overlap with the *I*, *J*, and *H* bands. The image size is ≈2.5′ × 1.7′. North is up and east to the left. The arrows indicate the positions of R145 and the star cluster R 136. The distance between R145 and R 136 is ≈1.3′, or in projection, ≈19 pc.

stars, whose powerful winds make it virtually impossible to estimate their surface gravities. Fortunately, massive stars ($M \gtrsim 8 \, M_\odot$) tend to exist in binary or multiple systems (Mason et al. 2009; Maíz Apellániz 2010; Oudmaijer & Parr 2010; Sana et al. 2012, 2014; Sota et al. 2014; Aldoretta et al. 2015).

Primarily as a result of mass-transfer, the evolutionary path of a star in a binary can greatly deviate from that of an identical star in isolation (Paczynski 1973; Langer 2012; de Mink et al. 2014). The impact and high frequency of binarity make binaries both indispensable laboratories for the study of massive stars and important components of stellar evolution. Hence, it is imperative to discover and study massive binary systems in the Galaxy and the Local Group.

R145 (BAT99 119, HDE 269928, Brey 90, VFTS 695) is a known massive binary situated in the famous Tarantula nebula in the Large Magellanic Cloud (LMC), about 19 pc away from the massive cluster R 136 in projection (see Fig. 1). The system's composite spectrum was classified WN6h in the original BAT99 catalog (Breysacher et al. 1999), which, according to this and past studies (e.g., Schnurr et al. 2009, S2009 hereafter), corresponds to the primary. The primary thus belongs to the class of late WR stars that have not yet exhausted their hydrogen content, and core H-burning is most likely still ongoing.

The system was speculated to host some of the most massive and luminous stars in the Local Group. Erroneously assuming a circular orbit, Moffat (1989) detected a periodic Doppler shift with a period of $P = 25.17$ d, concluding R145 to be an SB1 binary. A significantly different period of 158.8 ± 0.1 d was later reported by S009, who combined data from Moffat (1989) with their own and found a highly eccentric system. S009 could not derive a radial velocity (RV) curve for the secondary. However, they attempted to estimate the secondary's RV amplitude by looking for "resonance" velocity amplitudes that would strengthen the secondary's features in a spectrum formed by coadding the spectra in the secondary's frame of reference, under the assumption that the secondary is mainly an absorption-line star moving in antiphase to the primary star. Combined with the orbital inclination of $i = 38° \pm 9$ that they derived, their results tentatively implied that the system comprises two incredibly massive stars of ≈300 and ≈125 $M_\odot$,

making it potentially the most massive binary system known to date. For comparison, binary components of similar spectral type typically have masses ranging from ≈50 to ≈100 $M_\odot$ (e.g., WR 22, Rauw et al. 1996; WR 20a, Bonanos et al. 2004; Rauw et al. 2004; WR 21a, Niemela et al. 2008; Tramper et al. 2016; HD 5980, Koenigsberger et al. 2014; NGC 3603-A1, Schnurr et al. 2008a); masses in excess of 300 $M_\odot$ were so far only reported for putatively single stars (e.g., Crowther et al. 2010) based on comparison with evolutionary models.

With such high masses, signatures for wind-wind collisions (WWC) are to be expected (Moffat 1998). WWC excess emission can be seen photometrically as well as spectroscopically, and can thus also introduce a bias when deriving RVs. WWC signatures do not only reveal information on the dynamics and kinematics of the winds, but can also constrain the orbital inclination, which is crucial for an accurate determination of the stellar masses. Polarimetry offers a further independent tool to constrain orbital inclinations of binary systems (Brown et al. 1978). Both approaches are used in this study to constrain the orbital inclination *i*. For high inclination angles, photometric variability that is due to photospheric or wind eclipses can also be used to constrain *i* (e.g., Lamontagne et al. 1996). At the low inclination angle of R145 (see Sects. 4 and 7, as well as S2009), however, eclipses are not expected to yield significant constraints.

Using 110 high-quality Fibre Large Array Multi Element Spectrograph (FLAMES) spectra (Sect. 2), we are able to derive for the first time a double-lined spectroscopic orbit for R145. We identify lines that enable us to construct a reliable SB2 RV curve (Sect. 3). The majority of the spectra were taken as part of the VLT FLAMES-Tarantula survey (VFTS, Evans et al. 2011) and follow-up observations (PI: H. Sana). The study is conducted in the framework of the Tarantula Massive Binary Monitoring (TMBM) project (Almeida et al. 2017, Paper I hereafter).

The RVs of both components are fitted simultaneously with polarimetric data to obtain accurate orbital parameters (Sect. 4). In Sect. 5, we disentangle the spectrum into its constituent spectra. Using the disentangled spectra, an X-shooter spectrum, and additional observational material, we perform a multiwavelength spectroscopic analysis of the system using the Potsdam Wolf-Rayet (PoWR) model atmosphere code to derive the fundamental stellar parameters and abundances of the two stars (Sect. 6). An analysis of WWC signatures is presented in Sect. 7. A discussion of the evolutionary status of the system in light of our results is presented in Sect. 8. We conclude with a summary in Sect. 9.

2. Observational data

The FLAMES spectra (072.C-0348, Rubio; 182.D-0222, Evans; 090.D-0323, Sana; 092.D-0136, Sana) were secured between 2004 and 2014 with the FLAMES instrument mounted on the Very Large Telescope (VLT), Chile, partly in the course of two programs: the VLT FLAMES Tarantula Survey (Evans et al. 2011), and the TMBM project. They cover the spectral range 3960–4560 Å, have a typical signal-to-noise ratio (S/N) of 100, and a resolving power of $R \approx 8000$ (see Paper I for more information). The spectra were rectified using an automated routine that fits a piecewise first-order polynomial to the apparent continuum and cleaned from cosmic events using a dedicated Python routine we developed.

For the spectral analysis, we use an X-shooter (Vernet et al. 2011) spectrum (085.D-0704, PI: Sana) taken on 22 April 2010 ($\phi \approx 0.5$, i.e., apastron, with the phase calculated using the

Table 1. Derived orbital parameters.

Parameter	Value
$P_{\rm orb}$ [days]	158.760
T_0 [MJD]	$56\,022.6 \pm 0.2$
K_1 [km s^{-1}]	96 ± 3
K_2 [km s^{-1}]	95 ± 4
e	0.788 ± 0.007
$\omega [^\circ]$	61 ± 7
$M_{\rm orb,1} \sin^3 i\ [M_\odot]$	13.2 ± 1.9
$M_{\rm orb,2} \sin^3 i\ [M_\odot]$	13.4 ± 1.9
$a_1 \sin i\ [R_\odot]$	302 ± 10
$a_2 \sin i\ [R_\odot]$	299 ± 10
V_0 [km s^{-1}]	270 ± 5
$\Omega\ [^\circ]$	62 ± 7
$i\ [^\circ]$	39 ± 6
τ_*	0.10 ± 0.01
Q_0	-2.13 ± 0.02
U_0	0.58 ± 0.02
γ	0.87 ± 0.07
$M_{\rm orb,1}\ [M_\odot]$	53^{+40}_{-20}
$M_{\rm orb,2}\ [M_\odot]$	54^{+40}_{-20}
$a_1\ [R_\odot]$	480^{+90}_{-65}
$a_2\ [R_\odot]$	475^{+100}_{-70}

Notes. Derived orbital parameters from a simultaneous fit of the FLAMES RVs and the polarimetry. The period is fixed to the value found from the SB1 fitting using all published RVs for the primary (see Sect. 3)
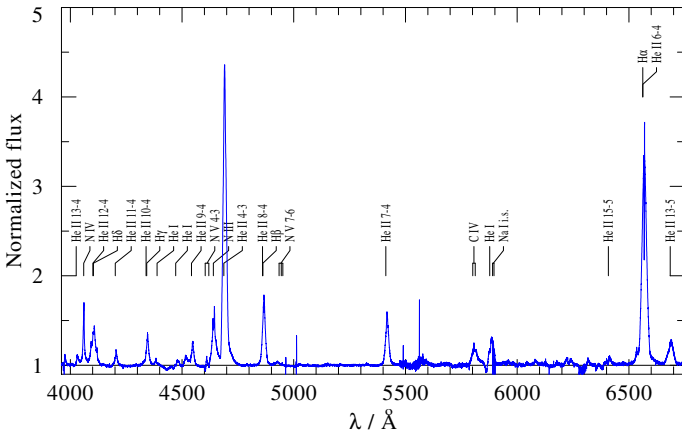
Fig. 2. Segment of the X-shooter spectrum of R145.

ephemeris given in Table 1 in Sect. 4). The spectrum covers the range 3000–25 000 Å. It has an $S/N \approx 100$ and a resolving power of $R \approx 7500$ in the spectral range 5500–10 000 Å and $R \approx 5000$ in the ranges 3000–5500 Å and 10 000–25 000 Å. It was rectified by fitting a first-order polynomial to the apparent continuum. A segment of the spectrum is shown in Fig. 2.

We make use of two high-resolution (HIRES), flux-calibrated International Ultraviolet Explorer (IUE) spectra available in the IUE archive. The two spectra (swp47847, PM048, PI: Bomans; swp47836, PM033, PI: de Boer) were obtained on 08
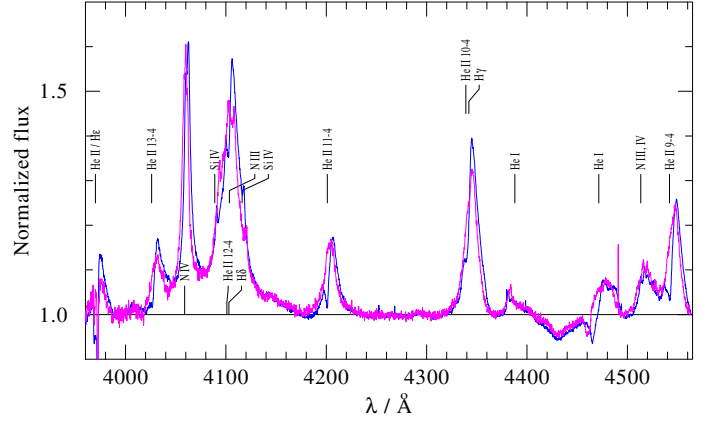
Fig. 3. Two FLAMES spectra taken shortly before ($\phi = -0.03$) and after ($\phi = 0.07$) periastron passage (extreme velocity amplitudes).

and 10 June 1993 at roughly $\phi = 0.7$ and were thus coadded to enhance the S/N. The coadded spectrum has a resolving power of $R \approx 10\,000$ and an $S/N \approx 10$. The spectrum was rectified using the composite PoWR model continuum (see Sect. 6).

Linear polarimetry was obtained between 1988 and 1990 at the 2.15 m Jorge Sahade telescope of the Complejo Astronómico El Leoncito (CASLEO) near San Juan, Argentina, with the Vatican Observatory Polarimeter (VATPOL, Magalhaes et al. 1984) and at the European Southern Observatory (ESO)/Max-Planck-Gesellschaft (MPG) 2.2 m telescope at La Silla, Chile, with Polarimeter with Instrumentation and Sky COmpensation (PISCO, Stahl et al. 1986). The data were obtained and originally used by S2009, where more details can be found.

3. SB2 orbit construction

As discussed in the introduction, R145 is a known SB1 binary. However, no previous studies could unambiguously isolate the secondary in the spectrum. Thanks to the moderate-resolution, high S/N of the FLAMES spectra, we are now able to detect spectral features that belong solely to the secondary and thus construct an SB2 orbit for the system.

Figure 3 shows two FLAMES spectra taken shortly before and after periastron ($\phi = 1$), where the RV differences are most extreme. It is readily seen that almost all spectral features shift in the same direction, that is, they stem primarily from one component, the primary. However, a closer inspection reveals that the secondary contributes to the N IV $\lambda4058$ emission and to some absorption features seen on top of He II and Balmer lines. Most importantly, the Si IV emission doublet at $\lambda\lambda4089, 4116$ moves in pure antiphase to the majority of the available spectral features, implying that the Si IV lines stem from the secondary alone. A zoom-in of Fig. 3, which focuses on the N IV $\lambda4058$ line and a member of the Si IV doublet, is shown in Fig. 4, where we also plot a spectrum taken close to apastron ($\phi \approx 0.5$).

To measure the RVs of the components in the individual FLAMES spectra, we performed a 1D cross-correlation algorithm to different spectral features in all available spectra. We tried two types of templates to cross-correlate with: a Gaussian, and the observations themselves. Both methods resulted in comparable values, although the Gaussians resulted in a worse fit quality, and are therefore omitted here.

We first used one of the FLAMES spectra as a template to cross-correlate with. A calibration of the template to the rest-frame using rest wavelengths λ_0 is known to lead to systematic errors since the barycenter of emission lines rarely coincides
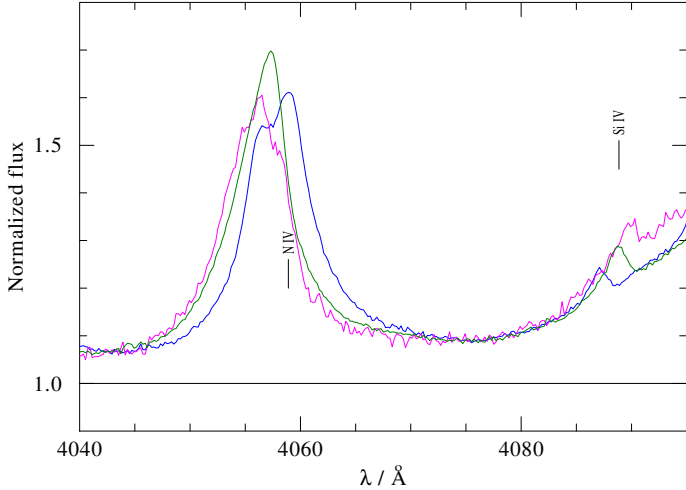
Fig. 4. Zoom-in of Fig. 3 showing the N IV and Si IV lines moving in anti-phase. A FLAMES spectrum at $\phi \approx 0.5$ is also shown (green). The primary dominates the N IV line, while the Si IV lines originate solely in the secondary. The spectra are shifted by the systemic LMC velocity of $270\,\mathrm{km\,s^{-1}}$.

with λ_0. To calibrate the template we therefore cross-correlated specific features with two preliminary PoWR models (see Sect. 6) calculated for the primary and secondary. We used the relatively symmetric and isolated N IV $\lambda 4058$ line and Si IV doublet to calibrate the templates of the primary and secondary, respectively. We note that, while the calibration to the restframe depends to a certain extent on our PoWR models, this only affects the systemic velocity V_0, and not the remaining orbital parameters.

Once the two template spectra were calibrated, we cross-correlated them against the individual FLAMES spectra, identifying the RV with the maximum of the cross-correlation function. For the primary, we measured RV shifts using the lines N IV $\lambda 4058$, He II $\lambda 4200$, He II $\lambda 4542$, and Hγ. The secondary contributes to all these lines, but its contribution is significantly smaller because of its lower mass-loss rate, and, judging by the cross-correlation fits, we do not expect that it influences the derived RVs. For the secondary, the Si IV doublet offers the most reliable way to track the secondary's motion, although the weak N III $\lambda 4379$ line also shows a clear antiphase behavior, and was therefore measured for RVs. The Si IV lines, which are blended with the Hδ line, were rectified relative to the contribution of the underlying Hδ emission for a more accurate derivation of the RVs.

With the preliminary velocities at hand, we created master templates for the primary and secondary by shifting the individual FLAMES spectra to the rest frame and coadding them. We then used these master templates to perform a new cross-correlation with the individual observations. The newly derived RVs differed only slightly from the previous ones and generally show less scatter. Errors on the RVs are estimated to be on the order of $10\,\mathrm{km\,s^{-1}}$ for the primary and $5\,\mathrm{km\,s^{-1}}$ for the secondary.

The derived RVs for the primary and secondary as a function of phase are shown in Figs. 5 and 6. The phase is calculated relative to our final orbital solution (Table 1). The measured RVs for the N IV (primary) and Si IV lines (secondary) are listed in Table A.1. The points are binned at intervals of 0.01 on phase (we note that often three FLAMES spectra were secured in a single observing night, cf. Table A.1).

From Fig. 5 it is evident that N IV $\lambda 4058$ and the He II $\lambda 4200$ and $\lambda 4542$ lines predict similar RVs, with N IV
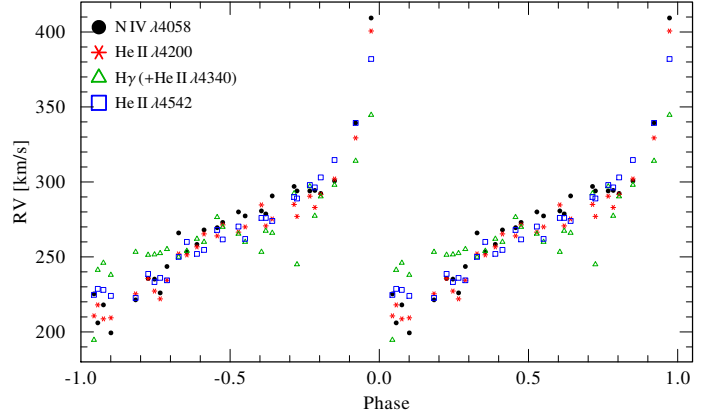
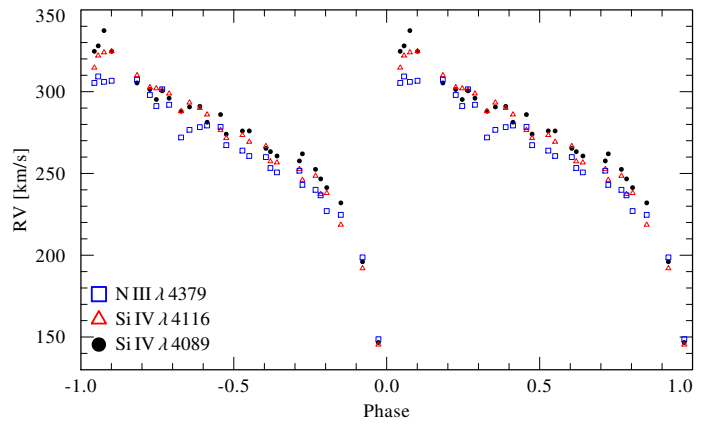**Fig. 5.** RVs for the primary component plotted over phase as measured for selected lines (see text).

Fig. 6. As Fig. 5, but for the secondary.

showing a slightly larger velocity amplitude. In contrast, Hγ (+ He II $\lambda 4340$) shows significantly more scatter and a phase-dependent deviation from the other lines. As we show in Sect. 7, the reason is probably a contamination of Hγ by WWC, as well as its large formation radii. The preliminary PoWR model for the primary (see Sect. 6) suggests that the He II lines form a few stellar radii away from the stellar surface, in contrast to the N IV line, which forms about ≈ 0.1 stellar radii away. This implies that the N IV line is more likely to represent the motion of the WR primary, and it is therefore used for the orbital fitting.

As for the secondary, we use the Si IV doublet. PoWR models calculated for the secondary (see Sect. 6) suggest that it forms very close to the stellar surface ($\approx 0.05\,R_*$ above the stellar surface), and should be very reliable for measuring the secondary's RVs. The two Si IV components agree well with each other and show a typical scatter of $\sigma \approx 7\,\mathrm{km\,s^{-1}}$ (Fig. 6). For the final RVs of the secondary, we average the results of these two lines.

In principle, we can derive orbital parameters using these velocities. However, the data only cover a few orbits and suffer from large gaps between them. We therefore combine old velocity measurements obtained by Moffat (1989) and S2009 for the primary with our datasets to assemble the longest possible time series, hence to obtain P with the highest possible accuracy. We note that the older velocities portray a significant systematic shift compared to the velocities derived here. This is mostly due to the different restframe calibration method used here. When performing the fitting, we therefore also fit for the systematic shifts for both sets of velocities. The SB1 fitting procedure is performed through a Levenberg-Marquardt technique using the

results of a Fourier analysis as a guess value for the initial period (Gosset et al. 2001).

From the SB1 fit, we derive the period P_{orb} = 158.760 ± 0.017 d, the epoch of periastron passage T_0[MJD] = 56 022.4 ± 0.8, the RV amplitude of the primary K_1 = 78 ± 3 km s^{-1}, the eccentricity e = 0.75 ± 0.01, and the argument of periastron ω = 61 ± 1°. Since the older velocities suffer from significantly larger errors, we do not adopt all orbital parameters derived, but only the period, which benefits significantly from the ≈30 yr of coverage. We do not find evidence for apsidal motion in the system, which may, however, be a consequence of the fact that the new data are of much higher quality than previous ones. In the next section, we analyze the polarimetric data simultaneously with the FLAMES data to better determine the orbital parameters and the orbital inclination. We note that the assumption here is that the period change caused by mass-loss from the system is negligible during these 30 yr. Since roughly $10^{-4.3}$ $M_\odot$ are lost from the system each year (see Sect. 6), approx. ΔM_{tot} = 0.001 $M_\odot$ were lost within 30 yr. The period change within 30 yr can be estimated through $P_i/P_f = (M_{tot,f}/M_{tot,i})^2$ (Vanbeveren et al. 1998). Assuming M_{tot} = 100 $M_\odot$ for an order-of-magnitude estimate, we obtain a difference in the period that is smaller than our error, and thus negligible.

4. Simultaneous polarimetry and RV fitting

Fitting the polarimetric data simultaneously with the RV data enables us to lay tighter constraints on the orbital parameters. Furthermore, as opposed to an RV analysis, polarimetry can yield constraints on the inclination i. As the orbital masses scale as $M_{orb} \propto \sin^3 i$, knowing i is crucial.

The polarimetric analysis is based on ideas developed by Brown et al. (1978, 1982), later corrected by Simmons & Boyle (1984). A similar analysis for the system was performed by S2009. As such, light emitted from a spherically symmetric star is unpolarized. While Thomson scattering off free electrons in the stellar wind causes the photons to be partially linearly polarized, the total polarization measured in the starlight cancels out if its wind is spherically symmetric. However, when the light of a star is scattered in the wind of its binary companion, the symmetry is broken, and some degree of polarization is expected. The degree of polarization depends on the amount and geometry of the scattering medium, which depends on the properties of the wind (e.g., mass-loss) and on the orbital phase.

In our case, the dominant source of free electrons would clearly be the wind of the primary WR star (see also Sect. 6), although some of the primary's light may also be scattered in the wind of the secondary star. We first assume that only the wind of the primary contributes to the polarization, given its dominance over that of the secondary. We will later relax this assumption. Following Robert et al. (1992), the Stokes parameters $U(\phi)$ and $Q(\phi)$ can be written as the sum of the (constant) interstellar polarizations U_0, Q_0 and phase-dependent terms:

$$U(\phi) = U_0 + \Delta Q(\phi) \sin \Omega + \Delta U(\phi) \cos \Omega$$
$$Q(\phi) = Q_0 + \Delta Q(\phi) \cos \Omega - \Delta U(\phi) \sin \Omega, \quad (1)$$

where Ω is the position angle of the ascending node, and $\Delta Q(\phi)$, $\Delta U(\phi)$ (in the case of spherically symmetric winds) are given by

$$\Delta U(\phi) = -2\tau_3(\phi) \cos i \sin(2\lambda(\phi))$$
$$\Delta Q(\phi) = -\tau_3(\phi) \left[\left(1 + \cos^2 i\right) \cos(2\lambda(\phi)) - \sin^2 i \right]. \quad (2)$$
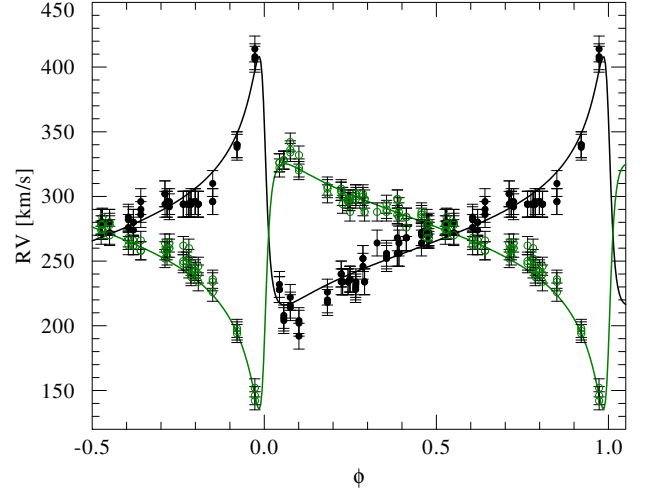

Fig. 7. Orbital solution plotted against the measured RVs for the N IV $\lambda 4058$ line (primary, black stars) and the averaged velocities of the Si IV $\lambda\lambda 4089, 4116$ doublet (secondary, green triangles).

Here, $\lambda(\phi) = \nu(\phi) + \omega - \pi/2$ is the longitude of the scattering source (primary) with respect to the illuminating source (secondary). ν is the true anomaly, ω is the argument of periastron. τ_3 is the effective optical depth of the scatterers (see Eqs. (4) and (5) in Robert et al. 1992) which scales with the (constant) total optical depth τ_* of the primary star (see Moffat et al. 1998). St.-Louis et al. (1988) assumed that $\tau_3(\phi) = \tau_* (a/D(\phi))^\gamma$, where $D(\phi)$ is the separation between the companions, and γ is a number on the order of unity. Brown et al. (1982) showed that $\gamma \approx 2$ in the case of a wind that is localized closely to the primary's stellar surface. However, this need not be the case for WR stars.

The free parameters involved in the polarimetry fitting are therefore $\Omega, i, \tau_*, Q_0, U_0$, and γ, as well as the orbital parameters P, ω, and e. This model can easily be generalized if both companions possess winds that can significantly contribute to the total polarization. In this case, τ_* is the sum of the optical depths of both stars, weighted with the relative light ratios (see Eq. (2) in Brown et al. 1982). The formalism may therefore be implemented here, with the only consequence that τ_* relates to the mass-loss rates of the two companions.

The simultaneous fitting of the FLAMES RVs and the polarimetric data is performed through a χ^2 minimization algorithm, with a relative weight given to the RV and polarimetric data chosen so that both types of data have a similar contribution to the total χ^2. Best-fit RV and Q/U curves are shown in Figs. 7 and 8. During the fitting procedure, the period is fixed to the value inferred from the combined RV sample (see Sect. 3). The corresponding best-fitting parameters are given in Table 1.

The inclination found in this study is very similar to that reported by S2009, which is not surprising given that we make use of the same polarimetric data. We note that clumps in the wind can generally enhance the scattering and may therefore lead to an overestimation of the inclination. The eccentricity is found to be hihger, e = 0.788 ± 0.007 as opposed to e = 0.70 ± 0.01 found by S2009. This also affects the remaining orbital parameters (cf. Table 5 in S2009). Most importantly, the orbital masses found here are much lower, $\approx 55^{+40}_{-20}$ $M_\odot$ for each component compared to $M_1 \gtrsim 300$ and $M_2 \gtrsim 125$ that were inferred by S2009. The reason for this discrepancy is the improved derivation of K_2 in our study. While we cannot supply a definitive reason for the erroneous derivation of K_2 by S2009, we suggest that it may be related to the fact that the secondary exhibits emission features
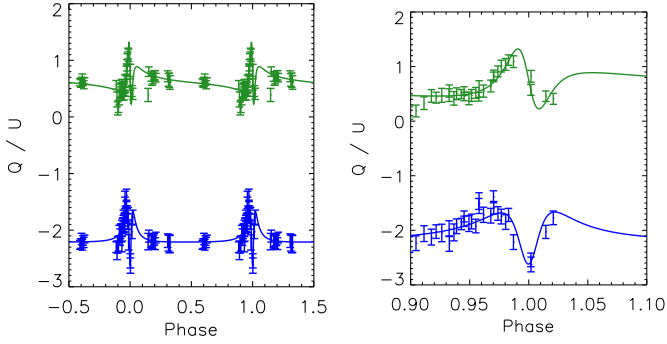
Fig. 8. Our polarimetric solution for Q (blue) and U (green) plotted against measured polarimetric data. The *right panel* is a zoom-in of the left panel around periastron passage.

as well as a blueshifted absorption. Furthermore, the spectra used in the latter study are of significantly lower quality than the FLAMES spectra.

The masses derived here are in much better agreement with the brightness of the system, as discussed by S2009. While the masses obtained here are close to the lower limit of what would be expected for these spectral types, as measured from eclipsing systems (e.g., Rauw et al. 2004; Bonanos et al. 2004; Schnurr et al. 2008b; Koenigsberger et al. 2014), they are not inconsistent, especially considering the errors. Moreover, given the bias of the polarimetric fitting toward higher inclination angles (e.g., Aspin et al. 1981; Wolinski & Dolan 1994), the masses derived here are very likely underestimated.

From Fig. 1 it is evident that the binary R145 is located outside the dense, massive cluster R 136. The projected separation between the system and the cluster is only ≈ 20 pc, which, accounting for an age of ≈ 2 Myr (cf. Table 3), implies an average velocity of a mere ≈ 10 km s^{-1}. The derived systemic velocity (cf. Table 1), which is comparable to the LMC mean velocity, would be consistent with a slow runaway ejected as a result of dynamical interactions within the cluster, as claimed for VFTS 682 (Banerjee et al. 2012). Alternatively, it may have formed in situ in the halo of the massive cluster R 136.

5. Spectral disentanglement

Using the orbital parameters given in Table 1 as an initial guess, we apply the disentanglement code SPECTANGULAR (Sablowski & Weber 2017) to the FLAMES spectra. The code performs the disentangling on a set of spectra in the wavelength domain rather than in the Fourier space (Hadrava 1995). Disentangling is coupled to an optimization algorithm on the orbital parameters. Hence, it provides revised orbital parameters and the separated component spectra.

It has been shown by Hadrava et al. (2009) that the disentangling can be successful as long as the line-profile variability is small compared to a mean profile and the orbital motion. However, these conditions are hardly met by the system under study, both owing to the intrinsic variability of WR stars (e.g., due to clumping) and owing to WWC. Indeed, we find that the orbital solution severely depends on the spectral domains used and the initial solution assumed. We therefore adopt the orbital parameters obtained in Sect. 4. In contrast, the resulting disentangled spectra are hardly influenced by the different solutions. We are therefore confident that the disentangled spectra obtained here represent the true spectra well, except in cases where the lines are heavily contaminated by variability.
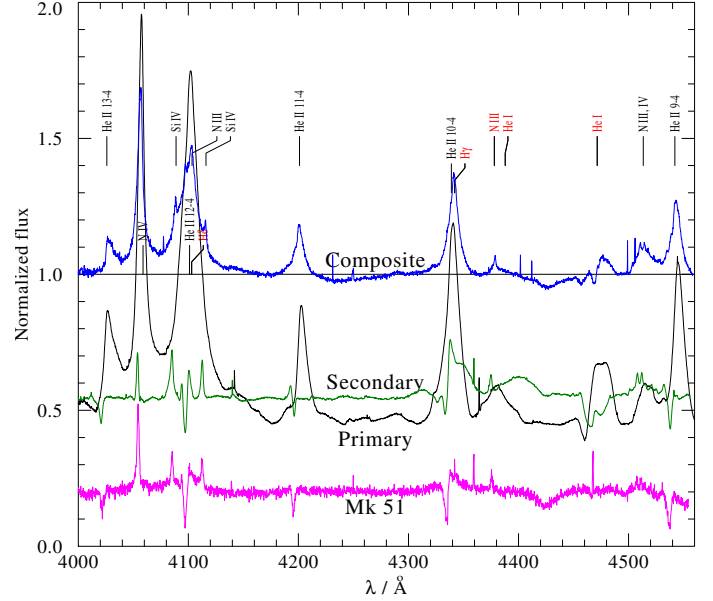
Fig. 9. Disentangled normalized spectra of the primary (black) and secondary (green), shifted to their relative light ratio. A composite FLAMES spectrum ($\phi \approx 0.5$) is shown for comparison (blue), as well as an observed normalized spectrum of Mk 51 for comparison with the secondary, shifted by –0.8 for clarity.

With no eclipses in the system, it is impossible for the disentanglement procedure to provide the light ratio of the primary and secondary components. The adopted light ratio influences the strength of the lines in the disentangled rectified spectra. Based on a calibration with equivalent widths (EWs) of putative single stars (see below), we estimate the light ratio to be $F_{v,2}/F_{v,tot} = 0.55 \pm 0.10$, where F_v is the visual flux in the Smith v band. This ratio is assumed for the rectified disentangled spectra, shown in Fig. 9.

The disentangled spectrum of the primary is consistent with it being of WN6h type. We compared the spectrum with two WN6h spectra in the LMC: BAT99 30 and BAT99 31. The adopted light ratio results in EWs of the He II lines that agree well with the two latter objects, but also results in an EW of the He I $\lambda4471$ line that is about three times larger, suggesting a strong He I excess in the system, probably originating in WWC (see Sect. 7).

The spectrum of the secondary is suggestive of a so-called slash star (Crowther & Walborn 2011). Unfortunately, the FLAMES spectra do not include diagnostic lines, which are important for the classification (e.g., Hβ, N V $\lambda\lambda4603$, 4619 and N III $\lambda\lambda\lambda4634$, 4640, 4642). Moreover, some lines, marked in red in Fig. 9, are strongly affected by WWC (see Sect. 7). This is especially significant for the secondary's spectrum, which generally shows weaker features than the primary. Especially the shape and strength of the lines in the range 4000–4200 Å is suggestive of an O3.5 If*/WN7 star, for which the star Melnick 51 (Mk 51) is a prototype. For comparison, we plot in Fig. 9 an observed normalized FLAMES spectrum of Mk 51 (P. Crowther, priv. comm.). The Si IV doublet is stronger in R145 than observed for MK51, and the N IV line weaker. However, the derived model and parameters for the secondary (see Sect. 6) are suggestive of the spectral class O3.5 If*/WN7. We therefore adopt this spectral class in this study. The light ratio adopted here is also chosen so that the EWs of the majority of the Balmer and He II lines agree with this spectral type (see Fig. 9).

6. Spectral analysis

The disentangled spectra, together with the high-quality X-shooter spectrum and the complementary UV and photometric data, enable us to perform a spectral analysis of both components. The spectral analysis is performed with the Potsdam Wolf-Rayet[1] (PoWR) model atmosphere code, applicable to any hot star (e.g., Shenar et al. 2015; Todt et al. 2015; Giménez-García et al. 2016). The code iteratively solves the comoving frame, non-local thermodynamic equillibrium (non-LTE) radiative transfer, and the statistical balance equations in spherical symmetry under the constraint of energy conservation, yielding the occupation numbers in the photosphere and wind. By comparing the output synthetic spectra to observed spectra, fundamental stellar parameters are derived. A detailed description of the assumptions and methods used in the code is given by Gräfener et al. (2002) and Hamann & Gräfener (2004). Only essentials are given here.

A PoWR model is defined by four fundamental stellar parameters: the effective temperature T_*, the surface gravity g_*, the stellar luminosity L, and the mass-loss rate $\dot{M}$. The effective temperature T_* is given relative to the stellar radius R_*, so that $L = 4\pi\sigma R_*^2 T_*^4$. R_* is defined at the model's inner boundary, fixed at mean Rosseland optical depth of $\tau_{\rm Ross} = 20$ (Hamann et al. 2006). The outer boundary is set to $R_{\rm max} = 1000\,R_*$. The gravity g_* relates to the radius R_* and mass M_* via the usual definition: $g_* = g(R_*) = G\,M_* R_*^{-2}$. We cannot derive g_* here because of the negligible effect it has on the wind-dominated spectra, and fix it to the value implied from the orbital mass.

The chemical abundances of the elements included in the calculation are prespecified. Here, we include H, He, C, N, O, Si, and the iron group elements dominated by Fe. The mass fractions $X_{\rm H}$, $X_{\rm C}$, and $X_{\rm N}$, and $X_{\rm Si}$ are derived in this work. Based on studies by Korn et al. (2000) and Trundle et al. (2007), we set $X_{\rm Fe} = 7 \times 10^{-4}$. Lacking any signatures associated with oxygen, we fix $X_{\rm O} = 5 \times 10^{-5}$ for both components. Values higher than 10^{-4} lead to spectral features that are not observed.

Hydrostatic equilibrium is assumed in the subsonic velocity regime (Sander et al. 2015), from which the density and velocity profiles follow, while a β-law (Castor et al. 1975) with $\beta = 1$ (e.g., Schnurr et al. 2008b) is assumed for the supersonic regime, defined by the β exponent and the terminal velocity v_∞. Optically thin clumps are accounted for using the microclumping approach (Hillier 1984; Hamann & Koesterke 1998), where the population numbers are calculated in clumps that are a factor of D denser than the equivalent smooth wind ($D = 1/f$, where f is the filling factor). Because optical WR spectra are dominated by recombination lines, whose strengths increase with $\dot{M}\sqrt{D}$, it is customary to parametrize their models using the so-called transformed radius (Schmutz et al. 1989),

$$R_{\rm t} = R_* \left[\frac{v_\infty}{2500\,{\rm km\,s^{-1}}} \left/ \frac{\dot{M}\sqrt{D}}{10^{-4}\,M_\odot\,{\rm yr^{-1}}} \right. \right]^{2/3}, \qquad (3)$$

defined so that EWs of recombination lines of models with given abundances, T_*, and $R_{\rm t}$ are approximately preserved, independently of L, $\dot{M}$, D, and v_∞.

The effective temperature of the primary is derived mainly based on the ionization balance of N III, N IV, and N V lines. For the secondary, the weakness of associated He I lines, as well as the presence of a strong N III component and a weak N IV component, constrain T_*. Once the temperatures and light ratio (see

Sect. 5) are constrained, mass-loss rates (or transformed radii) can be determined. For the primary, this is straightforward, while for the secondary, this can only be done approximately. The terminal velocity v_∞ is determined primarily from P-Cygni lines in the UV. Clumping factors are determined using electron scattering wings, primarily of He II $\lambda4686$. The hydrogen content is derived based on the balance of the Balmer series (He II + H) to pure He II lines. The remaining abundances are derived from the overall strengths of their associated lines.

The luminosity and reddening follow from a simultaneous fit to available photometry, adopting a distance of 50 kpc (Pietrzyński et al. 2013). We use U photometry from Parker et al. (1992), $BVRI$ photometry from Zacharias et al. (2012), JHK and IRAC photometry from the compilation of Bonanos et al. (2010), and WISE photometry from Cutri et al. (2013). The reddening is modeled using the reddening law published by Howarth (1983). In the latter, we find $R_V = 4.0 \pm 0.5$ is most consistent in reproducing the complete photometry, comparable to other stars in 30 Dorados (Maíz Apellániz et al. 2014), and we therefore fix $R_V = 4$ and fit for E_{B-V}. Maíz Apellániz et al. (2014) derived new laws for the 30 Dor region, but since the difference between these laws and older ones are negligible in the reddening regime involved here (see Figs. 11 and 12 in the latter paper), especially for the purpose of this study, these new laws are not implemented here.

The nitrogen abundance is found to be about a factor of two larger in both components compared to the typical LMC values (cf. Hainich et al. 2014), which is mostly due to the strong N III doublet at ≈4640 Å. However, this enhancement may be insignificant given the errors. Furthermore, to reproduce the Si IV doublet originating in the secondary, it is necessary to set $X_{\rm Si}$ to an abundance comparable to the Galactic one ($\approx$twice the typical LMC abundance, cf. Trundle et al. 2007). Since $X_{\rm Si}$ is not expected to change throughout the stellar evolution, we assume that silicon was initially overabundant, and fix the same value for the primary. Unfortunately, the poor quality of the UV data does not enable us to determine the abundance of the iron group elements. Because of the relatively large associated errors, we refrain from interpreting this apparent overabundance.

A comparison of the best-fitting models to the observed spectral energy distribution (SED) and normalized spectra is shown in Fig. 10. We note that the composite spectrum strongly underpredicts low-energy transitions such as He I lines. We show in Sect. 7 that these lines are expected to be strongly contaminated by WWC. The derived stellar parameters are listed in Table 2, where we also give the Smith and Johnson absolute magnitudes M_v and M_V, as well as the total extinction A_V. We also give upper limits derived for the projected and actual rotation velocity $v \sin i$ and $v_{\rm rot}$ for both components, as derived by comparing lines formed close to the stellar surface (N IV $\lambda4058$, Si IV doublet) to synthetic spectra that account for rotation in an expanding atmosphere, assuming corotation up to $\tau_{\rm Ross} = 2/3$ and angular momentum conservation beyond (cf. Shenar et al. 2014). Given the low inclination angle, these only place weak constraints on the actual rotation velocities $v_{\rm rot}$ of the stars. Errors are estimated from the sensitivity of the fit quality to variations of stellar parameters, or through error propagation.

Table 2 also lists stellar masses that are based on mass-luminosity relations calculated by Gräfener et al. (2011) for homogeneous stars. The relations depend on L and $X_{\rm H}$ alone. $M_{\rm MLR,hom}$ assumes the derived value of $X_{\rm H}$ in the core, that is, a homogeneous star. $M_{\rm MLR,He-b}$ assumes $X_{\rm H} = 0$, that is, the relation for pure He stars, which is a good approximation if the hydrogen-rich envelope is of negligible to moderate mass (see

---

[1] PoWR models of Wolf-Rayet stars can be downloaded at http://www.astro.physik.uni-potsdam.de/PoWR.html
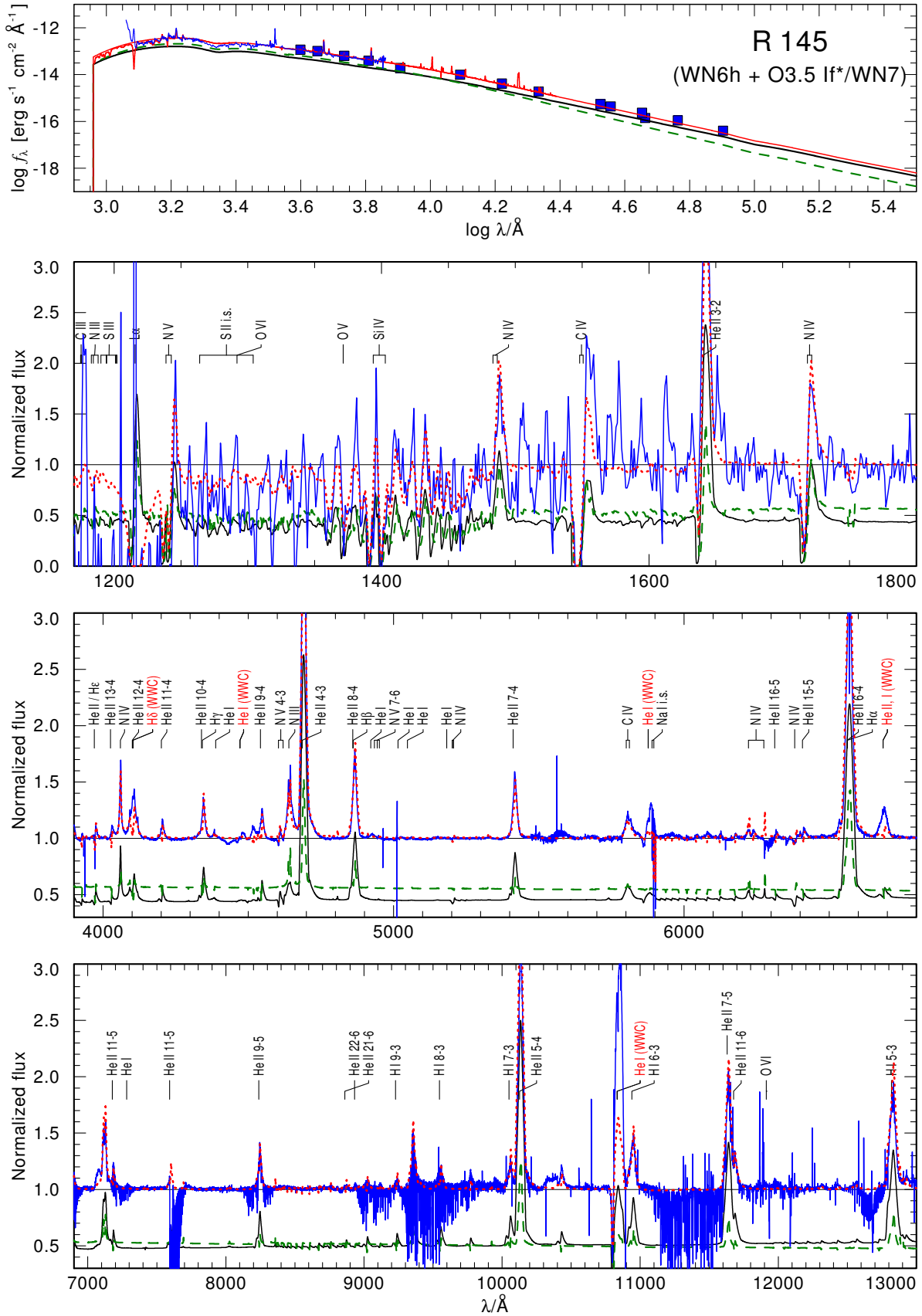
Fig. 10. Comparison between observed (blue squares and lines) SED (*upper panel*) and the normalized IUE and X-shooter spectra (*lower panel*) and the synthetic composite spectrum (red dotted line). The composite spectrum is the sum of the primary (black solid line) and secondary (green dashed line). The observed and modeled spectra in the UV are binned at 1 Å for clarity. Lines that are strongly affected by WWC are marked with red idents.

Table 2. Derived physical parameters for R145.

Parameter	Primary	Secondary
Spectral type	WN6h	O3.5 If*/WN7
T_* [K]	$50\,000 \pm 3000$	$43\,000 \pm 3000$
$\log L\,[L_\odot]$	6.35 ± 0.15	6.33 ± 0.15
$\log R_{\rm t}\,[R_\odot]$	1.05 ± 0.05	1.50 ± 0.15
v_∞ [km s^{-1}]	1200 ± 200	1000 ± 200
$R_*\,[R_\odot]$	20^{+6}_{-5}	26^{+9}_{-7}
$D\,[R_\odot]$	10 ± 0.3 dex	10 ± 0.3 dex
$\log \dot{M}\,[M_\odot\,{\rm yr}^{-1}]$	-4.45 ± 0.15	-4.9 ± 0.3
$v \sin i$ [km s^{-1}]	<200	<150
$v_{\rm rot}$ [km s^{-1}]	<350	<270
$X_{\rm H}$ (mass fraction)	0.4 ± 0.1	0.5 ± 0.2
$X_{\rm C}/10^{-4}$ (mass fraction)	0.8 ± 0.3	0.7 ± 0.4
$X_{\rm N}/10^{-3}$ (mass fraction)	8 ± 4	8 ± 4
$X_{\rm O}/10^{-4}$ (mass fraction)	$\lesssim 1$	$\lesssim 1$
$X_{\rm Si}/10^{-4}$ (mass fraction)	7 (fixed)	7 ± 3
M_v[mag]	-7.21 ± 0.25	-7.43 ± 0.25
M_V[mag]	-7.15 ± 0.25	-7.30 ± 0.25
$M_{\rm MLR,hom}[M_\odot]$	101^{+40}_{-30}	109^{+60}_{-40}
$M_{\rm MLR,He-b}[M_\odot]$	55^{+15}_{-12}	54^{+15}_{-12}
E_{B-V} [mag]	0.34 ± 0.01
A_V [mag]	1.4 ± 0.2

Fig. 11. Phased OGLE-III V- and I-band light-curve of R145.

discussion by Gräfener et al. 2011). If indeed $M_{\rm orb} \approx 55\,M_\odot \approx M_{\rm MLR,He-b}$, as is implied from Tables 1 and 2, the stars are most likely already core He-burning. However, this is very unlikely to be true for the secondary given its spectral type and luminosity. Rather, the orbital masses are very likely underestimated due to an overestimated inclination (e.g., Aspin et al. 1981), and may in fact be more similar to $M \approx 80{-}90\,M_\odot$, which is consistent with the upper boundary of our errors (see further discussion in Sect. 8).

Within errors, the derived physical parameters are in good agreement with the spectral types of the primary and secondary (cf. Crowther & Walborn 2011; Hainich et al. 2014). Bestenlehner et al. (2014) and Hainich et al. (2014) both analyzed R145 assuming a single component, which explains why they derived a luminosity in excess of $\log L = 6.5\,[L_\odot]$, about 0.2–0.3 dex higher than found here for the primary. Hainich et al. (2014) found a comparable effective temperature to that found for the primary in our study, while Bestenlehner et al. (2014) found a significantly lower temperature of 40 kK (comparable to the secondary), which is a consequence of attributing strong features stemming partially from the secondary (e.g., strong N III lines) to the primary. Similarly, the mass-loss rates derived here are different than in the previous studies because they did not account for line dilution and adopted incorrect luminosities. Given the careful binary analysis performed here, we are inclined to believe that our results represent the system much more accurately than previous studies.

7. Variability and wind-wind collision

Our results from the previous sections imply that the two binary components in R145 have significant stellar winds. In this case, it is expected that a cone-shaped wind-wind collision (WWC) zone would form, its tip situated along the line connecting the centers
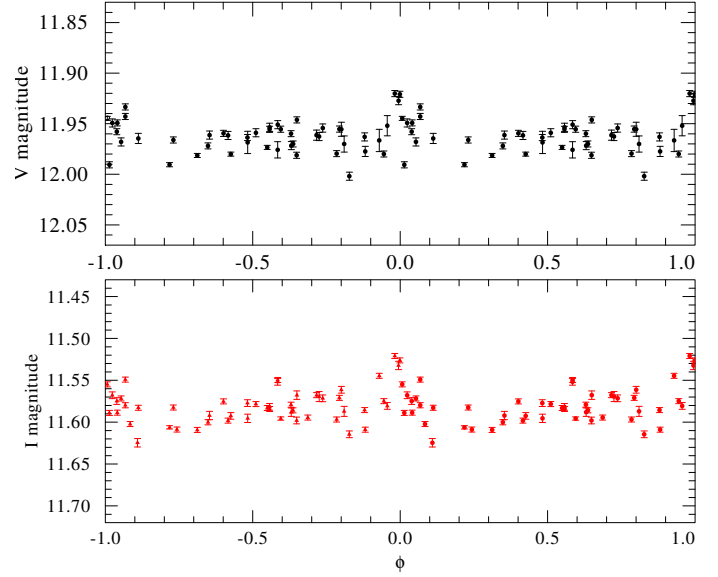
of the two stars at the point where the dynamical pressures of the two outflows equalize (Stevens et al. 1992; Moffat 1998). The temperatures in the immediate vicinity of the collision zone can reach a few 10^7 K. The plasma rapidly cools and emits radiation as it streams outward along the cone.

Observationally, the emission takes on two forms. On the one hand, WWC leads to excess emission that is photometrically visible, either in X-rays (Cherepashchuk 1976; Corcoran et al. 1996) or in non-thermal radio, infrared and optical (e.g., Williams et al. 1997). If the WWC occurs after the winds have reached their terminal velocities, the overall strength of the emission is expected to reach a maximum at periastron. In the adiabatic case, an inverse proportion with the separation D between the stars is predicted (Usov 1992). A sharper scaling ($\propto D^{-n}$, $n > 1$) is expected in highly radiative cases. On the other hand, WWC emission can also be spotted spectroscopically in addition to prominent emission lines in the optical, as the plasma cools off through recombination (e.g., Rauw et al. 1999; Hill et al. 2000; Sana et al. 2001). A spectroscopic analysis of the excess emission arising from the WWC zone can place strong constraints on the kinematics and inclination of the system (Luehrs 1997).

In Fig. 11, we show the V- and I-band light-curve of R145 (K. Ulaczyk, priv. comm.) obtained with the OGLE-III shallow survey (Ulaczyk et al. 2012), phased with the ephemeris in Table 1. A clear emission excess of $\approx 5\%$ during periastron passage is visible. Possible mechanisms that might cause a phase-dependent variability include wind eclipses, ellipsoidal deformations (e.g., Soszynski et al. 2004), and WWC. Wind eclipses are expected to cause a dip as the components align along the line of sight (phases 0.01 and 0.82), and while the outliers seen in Fig. 11 around these phases could indicate a wind eclipse, the data points are too sparse to tell. Ellipsoidal deformations could play a role, although it is unclear whether they are expected to be important for spectra that are wind-dominated. However, the emission excess seen during periastron is most easily explained by WWC. Given the sparseness of the data, however, we refrain from modeling the light curve.

To study the spectroscopic variability, we calculated the EWs of several lines in all 110 FLAMES spectra to check for periods present in the dataset. Figure 12 shows the EWs plotted versus phase, binned in intervals of $\Delta\phi = 0.01$. It is evident that lines
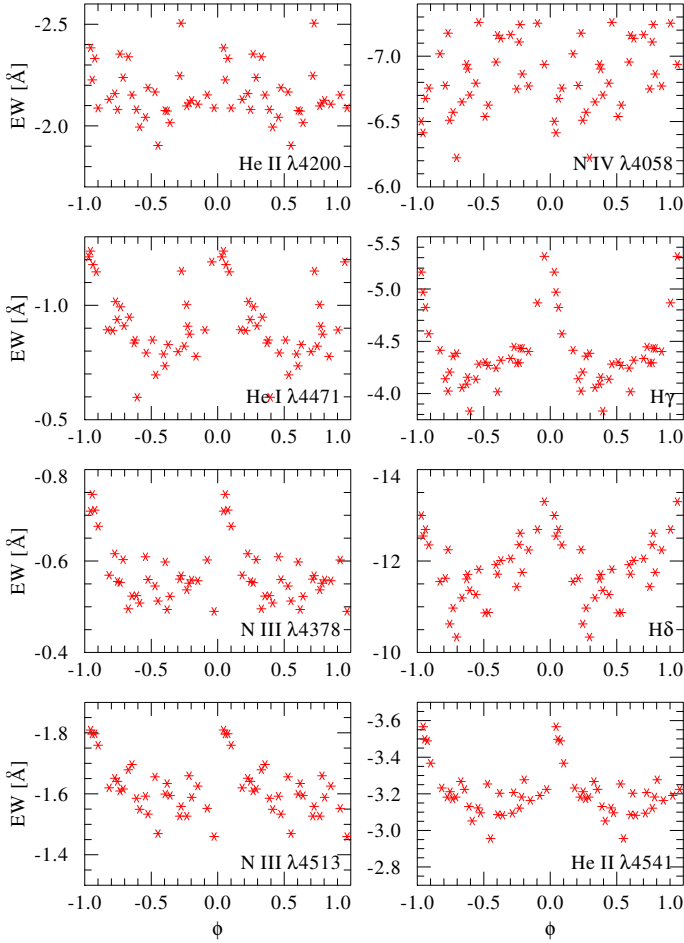
Fig. 12. EWs as a function of orbital phase ϕ measured for selected lines in the FLAMES spectra, binned at $\Delta\phi = 0.01$ intervals.
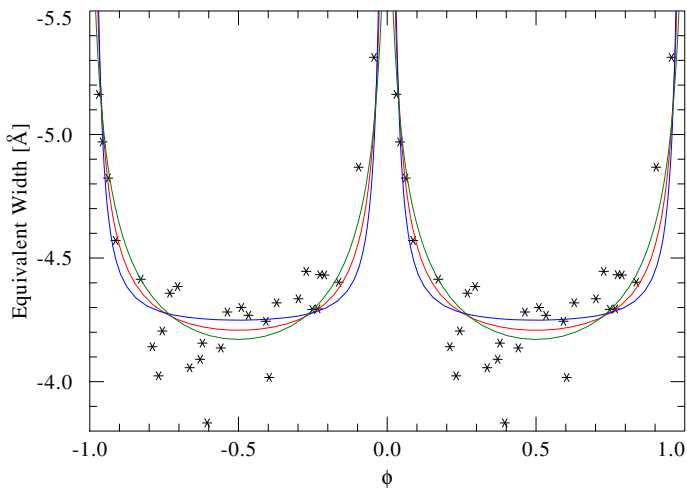

Fig. 13. Fits of the form $A_1 + B_1 D^{-2}$ (blue curve), $A_2 + B_2 D^{-1}$ (red curve), and $A_3 + B_3 D^{-\alpha}$ (green curve) to the data points describing the EW as a function of phase ϕ for the line $H\gamma$.

associated with low ionization stages such as He I, N III, and Balmer lines show a clear increase in the emission near periastron ($\phi = 0$). The largest increase in flux (factor of two) is seen at the He I λ4471 transition, followed by an increase of $\approx$40% for $H\gamma$. This is significantly more that observed for the continuum (see Fig. 11). This behavior is not seen at all in the He II λ4200
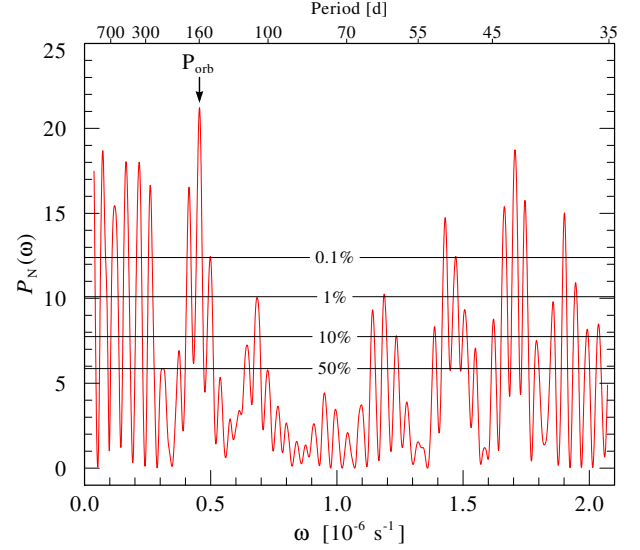

Fig. 14. Periodogram of the EWs of the $H\delta$ line. The periodogram was calculated from $\omega = 2\pi/T$ to $\omega = \pi N_0/T$ with a spacing $0.1/T$, where N_0 is the number of data points and T the total time of the observation. Various false-alarm probability levels are marked.

and N IV λ4058 lines, but is seen in the He II λ4541 line, possibly because it is blended with an N III component.

In Fig. 13, we plot the same data points as in Fig. 12 for $H\gamma$, but include three curves that correspond to functions of the form $A_1 + B_1 D^{-1}(\phi)$, $A_2 + B_2 D^{-2}(\phi)$, and $A_3 + B_3 D^{-\alpha}(\phi)$ with the constants A_i, B_i, and α chosen to minimize the sum of the squared differences χ^2. When leaving the exponent α as a free parameter, we obtain $\alpha \approx 0.25$. A similar test for the N III λ4378 line results in $\alpha \approx 1$, while for the He II λ4541 line, we obtain $\alpha \approx 1.2$. Given the intrinsic scatter in the EWs and the poor coverage during periastron, we cannot exclude the $1/D$ adiabatic dependence predicted by Usov (1992).

We checked for periodic signals on the EWs of the lines shown in Fig. 12. In most cases, we find significant detections of periods that agree with the orbital period. The remaining periods are found to be insignificant. In Fig. 14 a periodogram (Scargle 1982; Horne & Baliunas 1986) is shown as an example. The most prominent peak appears for a period of 158.9 ± 0.8 days, in very good agreement with the orbital period found (cf. Table 1). The occurrence of further apparently significant peaks is caused primarily by spectral leakage that is due to the unevenly spaced data (Horne & Baliunas 1986), as we confirmed by subtracting the main signal and constructing a second periodogram. We find a marginal detection of a further period of $P_2 \approx 21$ d, which may be related to stochastic variability in the system, but could also be spurious.

Figure 15 shows dynamic spectra calculated for three prominent lines: He I λ4471, $H\gamma$, and He II λ4200. The He I image is especially striking. There is a clear pattern of emission excess traveling from ≈ -600 km s^{-1} at $\phi \approx 0$ to ≈ 300 km s^{-1} at $\phi \approx 0.7$, and back again. This velocity amplitude clearly does not stem from the motion of the stars, which trace a different RV pattern and move at amplitudes of ≈ 100 km s^{-1}. In fact, the emission pattern is fully consistent with a rotating WWC cone, as suggested by Luehrs (1997). The two strong absorption dips seen close to periastron are also interesting; they likely occur when the cone arms tangentially sweep along the line of sight, thereby instantaneously increasing the optical depth.
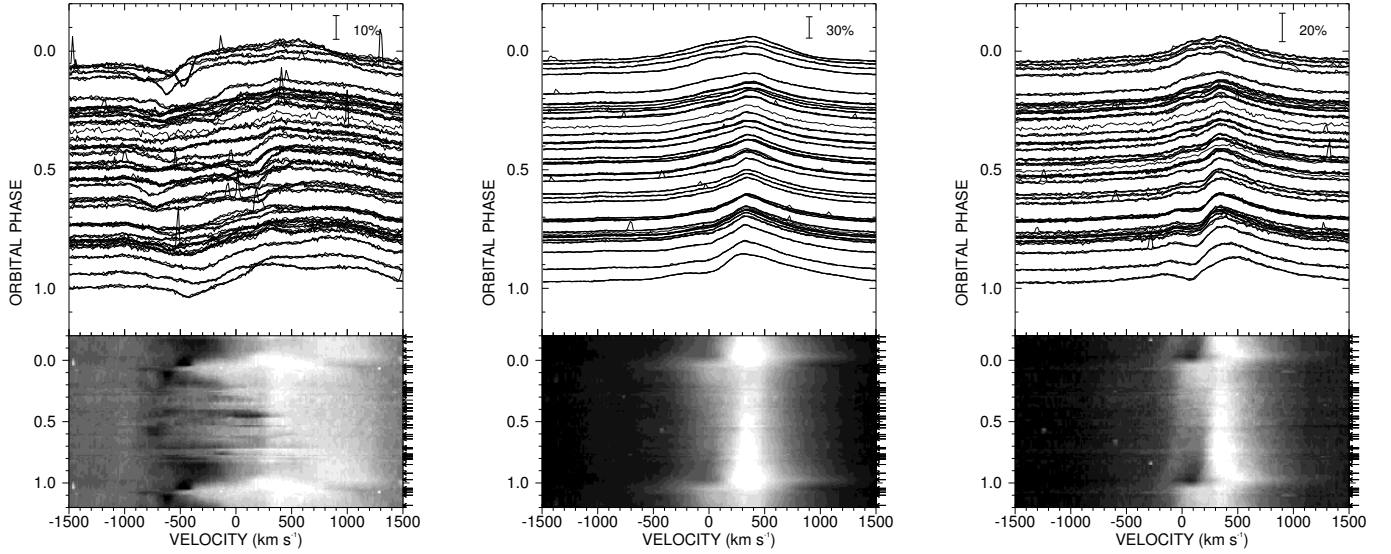
Fig. 15. Dynamic FLAMES spectra of He I λ4471 (*left*), Hγ (*center*), and He II λ4200 (*right*).

To proceed with a more quantitative analysis of the WWC zone, we follow the simple argumentation by Hill et al. (2000). Typically, very strong emission lines are needed for a quantitative analysis of WWC. However, our FLAMES spectra do not contain these lines. The most suitable line for the analysis is found to be He I λ4471. Owing to its weakness, only a rough analysis can be made here. The basic model predicts the dependence of the full width at half maximum (FW) of the emission excess profile and its mean RV as a function of orbital phase ϕ. FW(ϕ) and $\overline{\text{RV}}(\phi)$ can be written as

$$\text{FW}(\phi) = C_1 + 2\,v_{\text{str}}\,\sin\theta\,\sqrt{1 - \sin^2 i \cos^2(\phi - \delta\phi)}$$

$$\overline{\text{RV}}(\phi) = C_2 + v_{\text{str}}\cos\theta\sin i\cos(\phi - \delta\phi), \qquad (4)$$

where C_1 and C_2 are constants, v_{str} is the streaming velocity of the shocked gas, θ is the opening angle of the cone, i is the orbital inclination, and $\delta\phi$ is a phase shift introduced by Coriolis forces (see Fig. 6 in Hill et al. 2000).

An unbiased measurement of FW and RV was prevented by the low S/N of the line. Instead, the blue and red edge velocities of the emission excess, v_{b} and v_{r}, were estimated directly from the gray-scale plot shown in Fig. 15, from which FW and $\overline{\text{RV}}$ were calculated via $\text{FW}(\phi) = v_{\text{r}}(\phi) - v_{\text{b}}(\phi)$ and $\overline{\text{RV}}(\phi) = 0.5\,(v_{\text{b}}(\phi) + v_{\text{r}}(\phi))$. The stream velocity can be deduced from the position of the strong absorption dips around $\phi \approx 0$, seen at approximately $600\,\text{km s}^{-1}$. Accounting for the systemic velocity of the system ($\approx 300\,\text{km s}^{-1}$), we fix $v_{\text{str}} = 900\,\text{km s}^{-1}$. The value found here is slightly lower than the terminal velocity of the primary ($v_\infty \approx 1200\,\text{km s}^{-1}$), as is expected.

After fixing v_{str}, we determined the set of parameters C_1, C_2, θ, i, and $\delta\phi$ that minimize χ^2. For this purpose, a standard python routine (lmfit) is used. Our measurements of FW and $\overline{\text{RV}}$, compared with the best-fitting solutions, are shown in Fig. 16. We find $C_1 = 150 \pm 30\,\text{km s}^{-1}$, $C_2 = 450 \pm 20\,\text{km s}^{-1}$, $\theta = 73 \pm 6°$, $i = 40 \pm 5°$, and $\delta\phi = 8 \pm 3°$. The errors given here are strongly underestimated, as the true error lies in the measurement technique of the velocities and the simplified model.

It is immediately apparent that both our polarimetric analysis and the WWC analysis deliver almost identical inclinations. Admittedly, the value obtained here is biased by the method of
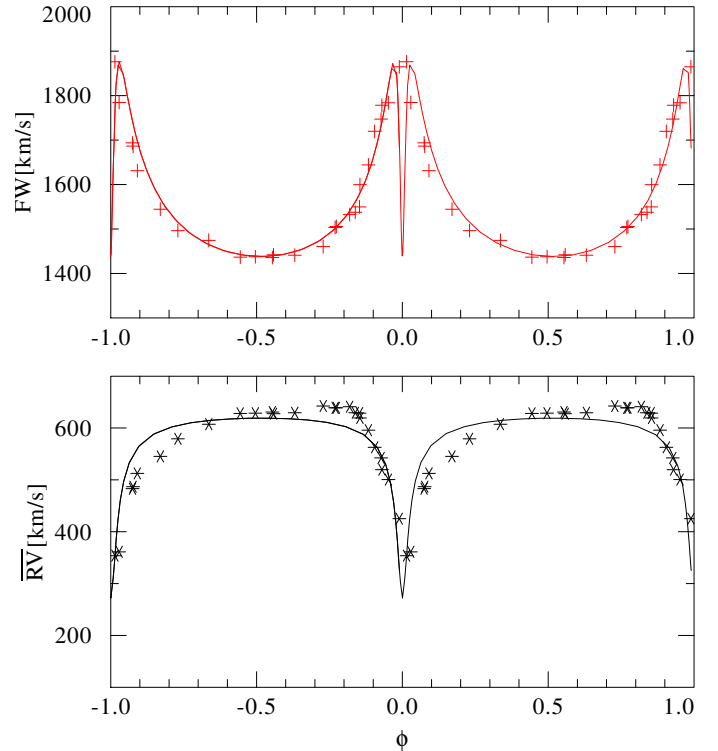

Fig. 16. Measured FW(ϕ) and $\overline{\text{RV}}(\phi)$ of the WWC emission excess profiles compared to their best-fitting models.

measuring v_{b} and v_{r}, and should therefore only be considered a further confirmation, rather as an independent derivation of i. It is also interesting to consider the opening angle θ. Usov (1995) showed that the opening angle can be calculated from

$$\theta = 2.1\left(1 - \frac{\eta^{2/5}}{4}\right)\eta^{1/3}, \qquad (5)$$

where $\eta = \dot{M}_2 v_{\infty,2} / (\dot{M}_1 v_{\infty,1})$ is the wind momentum ratio of both companions. Adopting our derived values from Table 2, we find $\eta = 0.48$, which yields $\theta = 76°$, in agreement with our results.

WWC may also manifest itself through powerful X-ray emission (Rauw & Naze 2016, and references therein). However, strong X-ray emission is not a necessary attribute of a colliding wind binary. Oskinova (2005) demonstrated that on average, the ratio between stellar bolometric and X-ray luminosity ($\log L_X/L_{bol} \approx -7$) is similar among Galactic massive binary and single stars, not without exceptions (e.g., Eta Car, Corcoran et al. 1995). R145 was detected by *Chandra* X-ray observatory (X-ray source designation CXOU J053857.06-690605.6, Townsley et al. 2014). The observations were taken over a period of 9 days around $T = 53\,760.7$ [MJD], corresponding to $\phi \approx 0.75$. Using E_{B-V} from Table 2 to estimate the interstellar neutral hydrogen column density, the observed count rate, and the median energy of the X-ray photons (Townsley et al. 2014), the X-ray luminosity of R145 in the 0.2–12 keV band is $L_X \approx 2 \times 10^{33}$ erg s^{-1}. This corresponds to[2] $\log L_X/L_{bol,tot} \approx -6.9$. Thus, R145 is not an especially luminous X-ray source, although it may be somewhat harder than a typical single star, as observed in other massive binaries (e.g., Nazé et al. 2011). Overall, the X-ray luminosity of R145 is similar to that of other detected massive stars in the LMC (e.g., Nazé et al. 2014).

The components of R145 follow a highly eccentric orbit. Therefore, modulations of the X-ray emission with orbital phases are expected. Previous snapshot observations are not suitable for detecting such orbital modulations. Dedicated monitoring X-ray observations of R145 are hoped to provide the required information about energetic processes in its interacting stellar winds.

8. System evolution

We now exploit the rich information derived here to constrain the evolutionary path of R145. Unfortunately, the derived orbital masses suffer from large uncertainties, even though we use high-quality data in this study (cf. Table 1). This is mainly due to the small inclination angle $i = 39°$, at which even a modest formal error of 6° translates into an error of $\approx 50\%$ in the mass. Moreover, due to non-linear biases, the value of i obtained here is very likely overestimated. Another hindrance is that the FLAMES spectra poorly cover the periastron passage (see Fig. 7), and so further monitoring would be desirable. Nevertheless, the masses of both components could be derived to an unprecedented precision, and set important constraints on the system.

The first question that comes to mind is whether the stars in this system have interacted in the past through mass-transfer. Evaluating the Roche-lobe radii through the Eggleton approximation (Eggleton 1983) using the semimajor axis a, we find $R_{RLOF,1} \approx R_{RLOF,2} \approx 360\,R_\odot$. At closest approach (periastron), the distance between the stars is $(1 - e)\,a$, and the Roche-lobe radii would be $R_{RLOF,1} \approx R_{RLOF,2} \approx 80\,R_\odot$. Thus, with radii of 20–30 $R_\odot$ (cf. Table 2), the stars are safely within their Roche-lobes, even at closest approach.

This does not imply, however, that the system has not interacted in the past. Although the primary is probably still core H-burning, it cannot be excluded that the primary exhibited larger radii in the past. How compact the primary was throughout its evolution is strongly related to how homogeneous it was. Stars undergoing quasi-homogeneous evolution (QHE) tend to maintain much higher temperatures throughout their evolution and therefore remain relatively compact (e.g., Brott et al. 2011). Homogeneity is typically enhanced in stellar evolution codes by

adopting high initial rotation velocities, which induce chemical mixing (Meynet & Maeder 2005; Heger & Langer 2000). Very massive stars may also be close to homogeneous simply because of their large convective cores and high mass-loss rates (e.g., Gräfener et al. 2011; Vink et al. 2015). If the primary underwent QHE, mass-transfer was probably avoided in the system. Otherwise, mass-transfer would have occurred in the system. The fact that the system is highly eccentric is indicative that no mass-transfer has occurred, since RLOF tends to efficiently circularize an orbit (Hurley et al. 2002).

8.1. Comparison with single star tracks

To gain more insight into the evolutionary course of the system, we compare the observables derived here to a set of evolution tracks calculated for single stars. These tracks are valid as long as the stars do not interact during their lifetime. We use tracks calculated by Brott et al. (2011) and Köhler et al. (2015) for initial masses in the range $5 \leq M_i \leq 500\,M_\odot$ and initial rotational velocities $0 \leq v_{rot,i} \lesssim 500$ km s^{-1} at a metallicity of $Z = 0.0047$, using the Bonn Evolutionary Code (BEC tracks hereafter), as well as tracks calculated with the Binary Population and Spectral Synthesis code (BPASS[3]) by Eldridge et al. (2011) and Eldridge & Stanway (2012) for homogeneous and non-homogeneous single stars with $5 \leq M_i \leq 150\,M_\odot$ and $Z = 0.004$ (BPASS tracks hereafter).

Finding the initial parameters and age that best reproduce the properties of the two components according to the BEC tracks is done most easily with the BONNSAI[4] Bayesian statistics tool (Schneider et al. 2014b). The disadvantage of the BEC tracks is that they, unlike the BPASS tracks, do not include post-core-H-burning phases. While the secondary is almost certainly core H-burning given its spectral type, this cannot be considered certain for the WR primary, although its properties and spectral type imply that it is most likely core H-burning as well (e.g., Hainich et al. 2014).

Figure 17 shows the Hertzsprung-Russell diagram (HRD) positions of the primary (A) and secondary (B) components of R145 compared to a selected number of BEC (left panel) and BPASS (right panel) evolution tracks. The colors code the amount of surface hydrogen content (see legend). We include QHE models as well as non-homogeneous models. For the BEC tracks, QHE is reached by high initial rotation rates; the tracks shown in Fig. 17 are calculated for $v_{rot,i} \approx 350$ km s^{-1}. The QHE BPASS tracks assume full homogeneity a priori; rotation is not considered in the BPASS code. We note that the QHE BEC tracks are not fully homogeneous.

8.1.1. BEC results

We first use the BONNSAI tool to find the initial parameters that best reproduce the observables T_*, L, X_H, and M_{orb} of the primary, accounting for the errors as found in this study. As anticipated, only tracks with high initial rotations ($v_{rot,i} \gtrsim 350$ km s^{-1}) can reproduce its HRD position (see left panel of Fig. 17); the non-homogeneous tracks terminate at low temperatures and do not return to high temperatures because hydrogen is then exhausted in the core. To obtain a consistent set of initial parameters for the secondary, we use the BONNSAI tool again to compare with the secondary's observables, but this time, we also use

---

[2] We compare with the total bolometric luminosity of the system because both stars are expected to intrinsically emit X-rays.

[3] bpass.auckland.ac.nz

[4] The BONNSAI web-service is available at www.astro.uni-bonn.de/stars/bonnsai
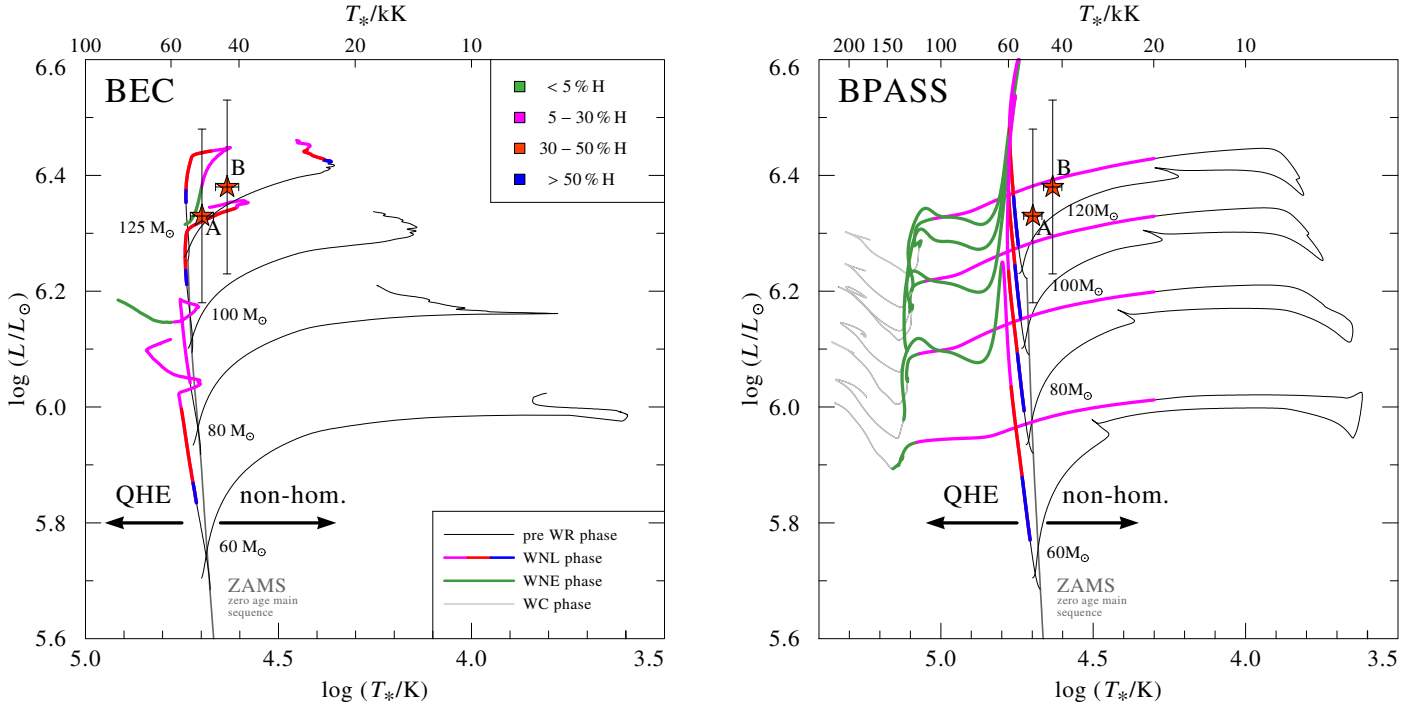
Fig. 17. HRD positions of the primary (A) and secondary (B) components of R145 compared to BEC (*left panel*) and BPASS (*right panel*) evolution tracks calculated for (near-)homogeneous and non-homogeneous evolution for LMC metallicities. The WR phase is defined for $X_H < 0.65$ and $T_* > 20$ kK. See text for details.

the primary age (and associated errors), as obtained from the BONNSAI tool.

The resulting initial masses and age (as derived for the primary) are shown in Table 3. The Table also lists the current masses and hydrogen content of the two components as predicted from the best-fitting evolutionary track. The initial rotations obtained by the BONNSAI tool for the primary and secondary are $v_{rot,i} = 410$ and $340\,\mathrm{km\,s^{-1}}$, respectively, while the predicted current rotational velocities are 240 and $260\,\mathrm{km\,s^{-1}}$, marginally consistent with the upper bounds given in Table 2. Since the non-homogeneous BEC models do not reproduce the HRD positions of the system components, we list only the corresponding QHE solution in Table 3.

8.1.2. BPASS results

A similar procedure is performed with the BPASS tracks. We use a χ^2 minimization algorithm to find the best-fitting homogeneous and non-homogeneous tracks and ages that reproduce the properties of the primary (see Eq. (3) in Shenar et al. 2016). Once a track and age for the primary is inferred, we repeat the procedure for the secondary, adopting the primary's age an associated error estimate that is based on the grid spacing. The corresponding initial parameters, ages, and current mass and surface hydrogen content are listed in Table 3. Because the BPASS tracks cover the whole evolution of the star, appropriate solutions can be found for the non-homogeneous case as well (see also right panel of Fig. 17). In Table 3 we also list the maximum radius $R_{max,1}$ reached by the primary throughout its evolution. This is meant to indicate whether the primary has exceeded its Roche-lobe radius in the past.

8.1.3. Indication of QHE

The BEC tracks and the BPASS tracks imply very similar initial parameters and ages in the QHE case for the two components. The tracks reproduce the observables reasonably well (compared to the errors), but the current masses predicted by the evolutionary tracks ($\approx 80-90\,M_\odot$) are higher than the orbital masses derived here ($\approx 55\,M_\odot$). Such masses would be obtained at an inclination of $\approx 33°$, which is roughly consistent with our formal error on i given in Table 1. The QHE scenario would therefore suggest that the actual masses are $\approx 80-90\,M_\odot$ per component.

For the non-QHE scenario, only the BPASS tracks can place meaningful constraints. In this scenario, the properties of the primary are reproduced when the evolution tracks return from the red to the blue, and He-core burning is initiated. This scenario is consistent with much lower current masses, closer to those derived here. However, significant discrepancy is obtained for the hydrogen content. More importantly, a comparison between the maximum radius reached by the primary and the Roche-lobe implies that when we adopt the non-homogeneous tracks, the primary overfilled its Roche-lobe in the past. We note that the separation increases with time because of mass-loss, making mass-transfer inevitable in the non-homogeneous case. In this scenario, binary interaction therefore has to be accounted for.

8.2. Binary tracks

We now use the set of tracks calculated with version 2.0 of the BPASS code (Eldridge et al. 2008) for $Z = 0.004$, which are non-homogeneous and account for mass-transfer. Each track is defined by an initial period P_i, an initial mass ratio $q_i = M_{i,2}/M_{i,1}$, and an initial mass for the primary $M_{i,1}$, calculated at intervals of 0.2 on $0 < \log P\,[\mathrm{d}] < 4$, 0.2 on $0 < q_i < 0.9$, and $10-20\,M_\odot$ on $10 < M_{i,1} < 150\,M_\odot$. The tracks do not include

Table 3. Comparison with best-fitting evolution tracks.

| | BEC | | BPASS | |
	QHE[a]	Non-hom.	QHE[b]	Binary[c]
$M_{i,1}$ $[M_\odot]$	105 ± 20	100 ± 20	100 ± 20	120 ± 20
$M_{i,2}$ $[M_\odot]$	91 ± 15	90 ± 20	90 ± 20	80 ± 20
$M_{cur,1}$ $[M_\odot]$	77^{+30}_{-15}	48 ± 10	96	58
$M_{cur,2}$ $[M_\odot]$	78^{+20}_{-10}	52 ± 10	85	113
Age [Myr]	2.3 ± 0.4	3.1 ± 0.3	2.1 ± 0.4	2.8 ± 0.4
$X_{H,1}$ (mass fr.)	0.3 ± 0.1	0.1 ± 0.1	0.4 ± 0.1	0.1 ± 0.1
$X_{H,2}$ (mass fr.)	$0.74^{+0}_{-0.25}$	0.1 ± 0.1	0.5 ± 0.1	–
$R_{max,1}$ $[R_\odot]$	40	1500	20	–

Notes. Initial parameters and predictions of best-fitting evolution tracks calculated for single stars experiencing homogeneous/non-homogeneous evolution. [a] QHE in the BEC tracks is reached via an initial rotation velocity of ≈ 350 km s^{-1} for both components, which best-reproduces the observables. [b] These tracks are fully homogeneous a-priori; rotation is not accounted for in the BPASS tracks. [c] The tracks are identical to the non-homogeneous tracks, but include mass-transfer. The initial period defining the best-fitting track is $P_i = 100$ d.

the hydrogen abundance of the secondary, so only a comparison with the primary's X_H is possible.

To determine the track that best reproduces the observables, we use a χ^2 minimization algorithm (see Eq. (4) in Shenar et al. 2016). We account here for T_*, L, M_{orb} for both components, X_H for the primary, the current period P, and the current mass-ratio $q = M_2/M_1 = K_1/K_2$. We note that we include the mass ratio because it has a much smaller formal error ($q = 1.01 \pm 0.07$) than the actual masses.

The parameters of the best-fitting binary track are given in the last column of Table 3. Even the best-fitting track results in a mass ratio of almost 2. The reason is that in all relevant tracks, RLOF from the primary to the secondary occurs, which tends to result in mass ratios significantly different than 1. The binary track also fails to reproduce the large hydrogen mass fraction inferred for the primary. Binary evolution tracks therefore only poorly in reproduce the system observables.

8.3. Outlook

To summarize, it appears that the system has evolved quasi-homogeneously, similarly to HD 5980 (Koenigsberger et al. 2014). This would suggest current masses of $\approx 80 \, M_\odot$ and initial masses of $M_1 \approx 105 \, M_\odot$ and $M_2 \approx 90 \, M_\odot$. The current generation of evolution models can attain QHE only by rapid initial rotation $v_i \gtrsim 350$ km s^{-1}. Admittedly, it might be argued that it is unlikely for both stars to be born with such high initial rotations (e.g., Ramírez-Agudelo et al. 2015). A possible resolution could lie in tidal interaction during periastron passage. The high eccentricity of the system yields a small separation between the components during periastron, which in turn may imply significant tidal mixing during periastron passage. As noted above, homogeneity can also be obtained by virtue of the large convective cores and strong mass-loss (Gräfener et al. 2011) of massive stars. Hence, the rotation that is needed for the BONN tracks may serve as a proxy for QHE rather than point at the actual physical mechanism responsible for homogeneity.

Assuming QHE indeed took place, there is no obvious reason to expect that the components would interact through RLOF in the future. This would be the case if the secondary would overfill

its Roche-lobe, which is currently hard to predict. If the components will indeed avoid interaction in the future, the system will very likely evolve into a wind-fed high-mass X-ray binary. With the help of fortunate kicks during core-collapse, the system could become close enough to merge within a Hubble time, emitting a gravitational wave event like those recently observed with LIGO (Abbott et al. 2016; Marchant et al. 2016).

9. Summary

We have performed an exhaustive analysis of the very massive system BAT99 119 (R145) in the LMC. Using high-quality FLAMES spectra, we detected and resolved for the first time lines from the secondary component and derived a first SB2 orbital solution for the system. The composite FLAMES spectral were disentangled into the constituent spectra of the two components, and a spectral analysis was performed to derive the physical parameters of the components. This enabled us to confirm the primary spectral type as WN6h, and to infer for the first time a spectral type for the secondary: O3.5 If*/WN7. A polarimetric analysis and a WWC analysis helped constrain the inclination of the system. Finally, a comparison with evolution tracks was conducted.

The system was previously speculated to host the most massive stars known ($M_1 > 300 \, M_\odot$, S2009). From our orbital + polarimetric analysis, we derive $q = M_2/M_1 = 1.01 \pm 0.07$ and masses $M_1 \approx M_2 \approx 55^{+40}_{-20} \, M_\odot$. Thus, although the masses suffer from large uncertainties, we can exclude masses higher than $100 \, M_\odot$ in the system.

We find clear evidence of WWC in the system. Interestingly, the signature of WWC is only clear in low-ionization transitions. We were only able to perform a rough quantitative spectroscopic analysis of the WWC spectral features because of the absence of very strong lines that are affected by WWC. The resulting inclination ($i = 40°$) is consistent with that obtained from polarimetry ($i = 39°$), and the half-opening angle ($\theta = 76°$) is consistent with the mass-loss rates and terminal velocities derived from the spectral analysis.

A comparison with quasi-homogeneous and non-homogeneous BEC and BPASS evolution tracks, the latter accounting for mass transfer as well, implies that quasi-homogeneous evolution (QHE) best describes the system. In this scenario, the components remain compact throughout their evolution and do not fill their Roche-lobes. Non-homogeneous evolution would imply mass transfer, and this in turn leads to mass ratios that are very different than found here (≈ 1), which is why we can exclude non-homogeneous evolution to a high degree of certainty. The high eccentricity found in this study ($e \approx 0.8$) is in line with the fact that the components did not interact by RLOF, which would tend to circularize the system. However, QHE is only consistent if the current masses are $\approx 80-90 \, M_\odot$, which is roughly the upper limit of our derived orbital masses. In any case, the initial masses of the stars are found to be $M_{1,i} \approx 105$ and $M_{2,i} \approx 90 \, M_\odot$.

Future spectroscopic and polarimetric observations are strongly encouraged to obtain more spectral phase coverage during periastron passage, which would constrain the orbital fit further and reduce uncertainties. A phase coverage of the red optical spectrum, as well as X-ray light curves, would be highly helpful in analyzing the WWC region to a much better degree of accuracy, enabling an accurate derivation of the inclination, and a detailed study of WWC in this important system.

References

Abbott, B. P., Abbott, R., Abbott, T. D., et al. 2016, Phys. Rev. Lett., 116, 061102
Aldoretta, E. J., Caballero-Nieves, S. M., Gies, D. R., et al. 2015, AJ, 149, 26
Almeida, L. A., Sana, H., Taylor, W., et al. 2017, A&A, 598, A84 (Paper I)
Andersen, J. 1991, A&ARv, 3, 91
Aspin, C., Simmons, J. F. L., & Brown, J. C. 1981, MNRAS, 194, 283
Banerjee, S., Kroupa, P., & Oh, S. 2012, ApJ, 746, 15
Bestenlehner, J. M., Vink, J. S., Gräfener, G., et al. 2011, A&A, 530, L14
Bestenlehner, J. M., Gräfener, G., Vink, J. S., et al. 2014, A&A, 570, A38
Bonanos, A. Z. 2009, ApJ, 691, 407
Bonanos, A. Z., Stanek, K. Z., Udalski, A., et al. 2004, ApJ, 611, L33
Bonanos, A. Z., Lennon, D. J., Köhlinger, F., et al. 2010, AJ, 140, 416
Bonnell, I. A., Bate, M. R., Clarke, C. J., & Pringle, J. E. 1997, MNRAS, 285, 201
Breysacher, J., Azzopardi, M., & Testor, G. 1999, A&AS, 137, 117
Brott, I., Evans, C. J., Hunter, I., et al. 2011, A&A, 530, A116
Brown, J. C., McLean, I. S., & Emslie, A. G. 1978, A&A, 68, 415
Brown, J. C., Aspin, C., Simmons, J. F. L., & McLean, I. S. 1982, MNRAS, 198, 787
Castor, J. I., Abbott, D. C., & Klein, R. I. 1975, ApJ, 195, 157
Cherepashchuk, A. M. 1976, Sov. Astron. Lett., 2, 138
Corcoran, M. F., Rawley, G. L., Swank, J. H., & Petre, R. 1995, ApJ, 445, L121
Corcoran, M. F., Stevens, I. R., Pollock, A. M. T., et al. 1996, ApJ, 464, 434
Crowther, P. A., Schnurr, O., Hirschi, R., et al. 2010, MNRAS, 408, 731
Crowther, P. A., & Walborn, N. R. 2011, MNRAS, 416, 1311
Cutri, R. M., et al. 2013, VizieR Online Data Catalog: II/328
de Mink, S. E., Sana, H., Langer, N., Izzard, R. G., & Schneider, F. R. N. 2014, ApJ, 782, 7
Eggleton, P. P. 1983, ApJ, 268, 368
Eldridge, J. J., & Stanway, E. R. 2012, MNRAS, 419, 479
Eldridge, J. J., Izzard, R. G., & Tout, C. A. 2008, MNRAS, 384, 1109
Eldridge, J. J., Langer, N., & Tout, C. A. 2011, MNRAS, 414, 3501
Evans, C. J., Taylor, W. D., Hénault-Brunet, V., et al. 2011, A&A, 530, A108
Giménez-García, A., Shenar, T., Torrejón, J. M., et al. 2016, A&A, 591, A26
Gosset, E., Royer, P., Rauw, G., Manfroid, J., & Vreux, J.-M. 2001, MNRAS, 327, 435
Gräfener, G., Koesterke, L., & Hamann, W.-R. 2002, A&A, 387, 244
Gräfener, G., Vink, J. S., de Koter, A., & Langer, N. 2011, A&A, 535, A56
Hadrava, P. 1995, A&AS, 114, 393
Hadrava, P., Šlechta, M., & Škoda, P. 2009, A&A, 507, 397
Hainich, R., Rühling, U., Todt, H., et al. 2014, A&A, 565, A27
Hamann, W.-R., & Gräfener, G. 2004, A&A, 427, 697
Hamann, W.-R., & Koesterke, L. 1998, A&A, 335, 1003
Hamann, W.-R., Gräfener, G., & Liermann, A. 2006, A&A, 457, 1015
Heger, A., & Langer, N. 2000, ApJ, 544, 1016
Hill, G. M., Moffat, A. F. J., St-Louis, N., & Bartzakos, P. 2000, MNRAS, 318, 402
Hillier, D. J. 1984, ApJ, 280, 744
Horne, J. H., & Baliunas, S. L. 1986, ApJ, 302, 757
Howarth, I. D. 1983, MNRAS, 203, 301
Hurley, J. R., Tout, C. A., & Pols, O. R. 2002, MNRAS, 329, 897
Koenigsberger, G., Morrell, N., Hillier, D. J., et al. 2014, AJ, 148, 62
Köhler, K., Langer, N., de Koter, A., et al. 2015, A&A, 573, A71
Korn, A. J., Becker, S. R., Gummersbach, C. A., & Wolf, B. 2000, A&A, 353, 655
Kroupa, P. 2001, MNRAS, 322, 231
Lamontagne, R., Moffat, A. F. J., Drissen, L., Robert, C., & Matthews, J. M. 1996, AJ, 112, 2227
Langer, N. 2012, ARA&A, 50, 107
Luehrs, S. 1997, PASP, 109, 504

Magalhaes, A. M., Benedetti, E., & Roland, E. H. 1984, PASP, 96, 383
Maíz Apellániz, J. 2010, A&A, 518, A1
Maíz Apellániz, J., Evans, C. J., Barbá, R. H., et al. 2014, A&A, 564, A63
Marchant, P., Langer, N., Podsiadlowski, P., Tauris, T. M., & Moriya, T. J. 2016, A&A, 588, A50
Mason, B. D., Hartkopf, W. I., Gies, D. R., Henry, T. J., & Helsel, J. W. 2009, AJ, 137, 3358
Massey, P., & Hunter, D. A. 1998, ApJ, 493, 180
Meynet, G., & Maeder, A. 2005, A&A, 429, 581
Moffat, A. F. J. 1989, ApJ, 347, 373
Moffat, A. F. J. 1998, Ap&SS, 260, 225
Moffat, A. F. J., Marchenko, S. V., Bartzakos, P., et al. 1998, ApJ, 497, 896
Nazé, Y., Broos, P. S., Oskinova, L., et al. 2011, ApJS, 194, 7
Nazé, Y., Petit, V., Rinbrand, M., et al. 2014, ApJS, 215, 10
Niemela, V. S., Gamen, R. C., Barbá, R. H., et al. 2008, MNRAS, 389, 1447
Oey, M. S., & Clarke, C. J. 2005, ApJ, 620, L43
Oskinova, L. M. 2005, MNRAS, 361, 679
Oskinova, L. M., Steinke, M., Hamann, W.-R., et al. 2013, MNRAS, 436, 3357
Oudmaijer, R. D., & Parr, A. M. 2010, MNRAS, 405, 2439
Paczynski, B. 1973, in Wolf-Rayet and High-Temperature Stars, eds. M. K. V. Bappu, & J. Sahade, IAU Symp., 49, 143
Parker, J. W., Garmany, C. D., Massey, P., & Walborn, N. R. 1992, AJ, 103, 1205
Pietrzyński, G., Graczyk, D., Gieren, W., et al. 2013, Nature, 495, 76
Ramírez-Agudelo, O. H., Sana, H., de Mink, S. E., et al. 2015, A&A, 580, A92
Rauw, G., & Naze, Y. 2016, Adv. Space Res., 58, 761
Rauw, G., Vreux, J.-M., Gosset, E., et al. 1996, A&A, 306, 771
Rauw, G., Vreux, J.-M., & Bohannan, B. 1999, ApJ, 517, 416
Rauw, G., De Becker, M., Nazé, Y., et al. 2004, A&A, 420, L9
Robert, C., Moffat, A. F. J., Drissen, L., et al. 1992, ApJ, 397, 277
Sablowski, D. P., & Weber, M. 2017, A&A, 597, A125
Salpeter, E. E. 1955, ApJ, 121, 161
Sana, H., Rauw, G., & Gosset, E. 2001, A&A, 370, 121
Sana, H., de Mink, S. E., de Koter, A., et al. 2012, Science, 337, 444
Sana, H., Le Bouquin, J.-B., Lacour, S., et al. 2014, ApJS, 215, 15
Sander, A., Shenar, T., Hainich, R., et al. 2015, A&A, 577, A13
Scargle, J. D. 1982, ApJ, 263, 835
Schmutz, W., Hamann, W.-R., & Wessolowski, U. 1989, A&A, 210, 236
Schneider, F. R. N., Izzard, R. G., de Mink, S. E., et al. 2014a, ApJ, 780, 117
Schneider, F. R. N., Langer, N., de Koter, A., et al. 2014b, A&A, 570, A66
Schnurr, O., Casoli, J., Chené, A.-N., Moffat, A. F. J., & St-Louis, N. 2008a, MNRAS, 389, L38
Schnurr, O., Moffat, A. F. J., St-Louis, N., Morrell, N. I., & Guerrero, M. A. 2008b, MNRAS, 389, 806
Schnurr, O., Moffat, A. F. J., Villar-Sbaffi, A., St-Louis, N., & Morrell, N. I. 2009, MNRAS, 395, 823
Shenar, T., Hamann, W.-R., & Todt, H. 2014, A&A, 562, A118
Shenar, T., Oskinova, L., Hamann, W.-R., et al. 2015, ApJ, 809, 135
Shenar, T., Hainich, R., Todt, H., et al. 2016, A&A, 591, A22
Simmons, J. F. L., & Boyle, C. B. 1984, A&A, 134, 368
Soszynski, I., Udalski, A., Kubiak, M., et al. 2004, Acta Astron., 54, 347
Sota, A., Maíz Apellániz, J., Morrell, N. I., et al. 2014, ApJS, 211, 10
St.-Louis, N., Moffat, A. F. J., Drissen, L., Bastien, P., & Robert, C. 1988, ApJ, 330, 286
Stahl, O., Buzzoni, B., Kraus, G., et al. 1986, The Messenger, 46, 23
Stevens, I. R., Blondin, J. M., & Pollock, A. M. T. 1992, ApJ, 386, 265
Todt, H., Sander, A., Hainich, R., et al. 2015, A&A, 579, A75
Torres, G., Andersen, J., & Giménez, A. 2010, A&ARv, 18, 67
Townsley, L. K., Broos, P. S., Garmire, G. P., et al. 2014, ApJS, 213, 1
Tramper, F., Sana, H., Fitzsimons, N. E., et al. 2016, MNRAS, 455, 1275
Trundle, C., Dufton, P. L., Hunter, I., et al. 2007, A&A, 471, 625
Ulaczyk, K., Szymański, M. K., Udalski, A., et al. 2012, Acta Astron., 62, 247
Usov, V. V. 1992, ApJ, 389, 635
Usov, V. V. 1995, in Wolf-Rayet Stars: Binaries; Colliding Winds; Evolution, eds. K. A. van der Hucht, & P. M. Williams, IAU Symp., 163, 495
Vanbeveren, D., De Loore, C., & Van Rensbergen, W. 1998, A&ARv, 9, 63
Vernet, J., Dekker, H., D'Odorico, S., et al. 2011, A&A, 536, A105
Vink, J. S. 2015, Very Massive Stars in the Local Universe, Astrophysics and Space Science Library, 412
Vink, J. S., Heger, A., Krumholz, M. R., et al. 2015, Highlights of Astronomy, 16, 51
Williams, P. M., Dougherty, S. M., Davis, R. J., et al. 1997, MNRAS, 289, 10
Wolinski, K. G., & Dolan, J. F. 1994, MNRAS, 267, 5
Zacharias, N., Finch, C. T., Girard, T. M., et al. 2012, VizieR Online Data Catalog: I/322

Appendix A: RV measurements

Table A.1. RVs for primary (N IV) and secondary (Si IV) components.

Spectrum	MJD	ϕ	N IV RV [km s^{-1}]	Si IV RV [km s^{-1}]
1	54 794.18	0.27	230	302
2	54 794.20	0.27	256	286
3	54 794.24	0.27	220	298
4	54 794.32	0.27	234	300
5	54 798.29	0.29	234	288
6	54 798.31	0.29	234	298
7	54 804.07	0.33	266	288
8	54 836.13	0.53	280	284
9	54 836.16	0.53	280	278
10	54 836.18	0.53	280	274
11	54 836.20	0.53	280	274
12	54 867.05	0.72	292	264
13	54 867.07	0.72	296	260
14	55 108.27	0.24	234	296
15	55 108.29	0.24	234	298
16	56 210.35	0.18	226	308
17	56 210.37	0.18	220	306
18	56 210.38	0.18	218	302
19	56 217.33	0.23	234	300
20	56 217.34	0.23	234	300
21	56 217.35	0.23	234	294
22	56 243.34	0.39	256	288
23	56 243.35	0.39	252	300
24	56 243.36	0.39	256	292
25	56 256.26	0.47	270	278
26	56 256.27	0.47	280	272
27	56 256.28	0.47	276	268
28	56 257.13	0.48	270	268
29	56 257.14	0.48	270	278
30	56 257.15	0.48	272	280
31	56 277.31	0.61	282	268
32	56 277.32	0.61	284	266
33	56 277.33	0.61	276	262
34	56 283.05	0.64	296	258
35	56 283.06	0.64	268	298
36	56 283.07	0.64	290	258
37	56 294.20	0.71	302	258
38	56 294.21	0.71	302	264
39	56 294.23	0.71	294	252
40	56 295.18	0.72	296	254
41	56 295.19	0.72	294	258
42	56 295.21	0.72	294	260
43	56 304.24	0.77	294	250
44	56 305.23	0.78	294	252
45	56 305.24	0.78	294	244
46	56 305.26	0.78	294	260
47	56 306.22	0.79	294	238
48	56 306.23	0.79	268	276
49	56 306.24	0.79	294	246
50	56 308.15	0.80	296	242
51	56 308.17	0.80	296	242
52	56 308.18	0.80	280	244
53	56 316.21	0.85	296	234
54	56 316.22	0.85	296	226

Table A.1. continued.

Spectrum	MJD	ϕ	N IV RV [km s^{-1}]	Si IV RV [km s^{-1}]
55	56 316.23	0.85	310	236
56	56 347.01	0.04	222	326
57	56 347.03	0.04	232	326
58	56 347.04	0.04	222	322
59	56 349.02	0.06	206	328
60	56 349.03	0.06	208	328
61	56 349.05	0.06	204	328
62	56 352.02	0.08	224	342
63	56 352.04	0.08	268	284
64	56 352.05	0.08	214	334
65	56 356.00	0.10	268	284
66	56 356.02	0.10	192	332
67	56 356.03	0.10	202	322
68	56 571.34	0.46	264	284
69	56 571.35	0.46	272	288
70	56 571.37	0.46	406	142
71	56 571.38	0.46	270	286
72	56 582.34	0.53	280	270
73	56 582.35	0.53	280	274
74	56 582.37	0.53	280	278
75	56 586.25	0.55	280	280
76	56 586.26	0.55	272	270
77	56 586.27	0.55	280	278
78	56 597.23	0.62	236	298
79	56 597.24	0.62	276	262
80	56 597.25	0.62	280	262
81	56 620.26	0.76	294	250
82	56 620.27	0.76	294	248
83	56 620.28	0.76	294	262
84	56 627.16	0.81	294	234
85	56 627.18	0.81	294	246
86	56 627.19	0.81	338	196
87	56 645.04	0.92	256	298
88	56 645.05	0.92	340	194
89	56 645.07	0.92	338	196
90	56 653.28	0.97	414	152
91	56 653.29	0.97	408	146
92	56 653.30	0.97	406	142
93	56 693.11	0.22	234	304
94	56 693.12	0.22	238	306
95	56 693.13	0.22	240	304
96	56 697.16	0.25	236	296
97	56 697.17	0.25	236	288
98	56 697.19	0.25	236	298
99	56 703.13	0.29	252	300
100	56 703.14	0.29	252	302
101	56 703.16	0.29	246	292
102	56 714.02	0.36	252	288
103	56 714.03	0.36	252	288
104	56 714.05	0.36	252	290
105	56 719.02	0.39	256	286
106	56 719.03	0.39	256	298
107	56 719.04	0.39	268	298
108	56 723.17	0.41	268	284
109	56 723.18	0.41	268	276
110	56 723.20	0.41	268	284